Mass Loaded Tensioned Mechanical Resonators

by

Sanjay Kumar Keshava

A thesis submitted to the
Faculty of the Honors Program of the
University of Colorado Boulder in partial fulfillment
for a Latin honors designation with the degree of
Bachelors of Science in Engineering Physics
Department of Physics

Defended 4th April, 2023

Thesis Advisor:
Prof. Cindy Regal, JILA and Department of Physics

Honors Committe Members:
Prof. John Cumalat, Physics Honors Council Representative, Department of Physics
Prof. András Gyenis, Outside Reader, Department of Electrical, Computer & Energy Engineering

This thesis entitled:
Mass Loaded Tensioned Mechanical Resonators
written by Sanjay Kumar Keshava
has been approved for the Department of Physics

Prof. Cindy Regal
Thesis Advisor, JILA and Department of Physics

Prof. John Cumalat
Physics Honors Council Representative, Department of Physics

Prof. András Gyenis
Outside Reader, Department of Electrical, Computer & Energy Engineering

Date ____________________

The final copy of this thesis has been examined by the signatories, and we find that both the content and the form meet acceptable presentation standards of scholarly work in the above mentioned discipline.

Kumar Keshava, Sanjay (Bachelors of Science in Engineering Physics)

Mass Loaded Tensioned Mechanical Resonators

Directed by Prof. Cindy Regal

Thesis Advisor, JILA and Department of Physics

Highly tensioned micromechanical and nanomechanical resonators have enabled novel experiments in quantum optomechanics and numerous applications in the field of precision sensing. This is in part due to engineering efforts that have allowed for resonator modes with ultrahigh quality factors. Typically, sensing applications require functionalizing resonators by adding local mass to them. However, this may dramatically lower the resonator mode quality factor, and hence its sensitivity. This thesis studies the effect of a local mass load on the shape and quality factor of a tensioned resonator mode. Through analytical models, finite element analysis, and tabletop experiments, we show that in the limit of a large mass load, the resonator mode quality factor saturates. This effect paves the way for engineering resonators with improved sensitivity for certain applications such as magnetic force detection, accelerometry, and gravitational force sensing.

Dedication

This thesis is dedicated to my mum, dad, and brother.

Acknowledgements

I would first like to thank Professor Cindy Regal for giving me the opportunity to work in her group. She ensured that I had meaningful projects to work on throughout my undergraduate career, and always gave me the freedom to pursue my own ideas. This made research very enjoyable. I have learned a lot from her about how to ask the right questions and look at the big picture without getting caught up in all the technical details. She has always been invested in my success and I could not have imagined a better advisor.

Next, I must thank Chris and Ravid. Chris spent countless hours teaching me all sorts of things and patiently answered my endless stream of questions when I initially joined the group. When working on a problem, he always gave me enough to go on, but allowed me to make mistakes and pushed me to learn things on my own, and this has helped me to become more independent. I learned a lot from him about mechanics, optics, COMSOL, working in a clean room, and physics in general. From Ravid, I learned about the importance of extracting science from experiments that seemed to be going nowhere. It was also an enlightening experience to work closely with him on the mass-loading paper, and it has helped me better understand what it takes to write a paper and get through the peer-review process. I should also thank Chris and Ravid for putting up with all my craziness in general and especially my constant flurry of world-changing ideas (such as building a quantum computer to mine bitcoins). More recently, it has been great to work with the new grad student Sofia (thanks for all the homework help). Although we have only communicated via Discord and seen each other exactly once, I am sure the newest undergraduate Ruomu will be a great addition to the group. I must also thank the M2O members, especially Max and Luca.

Special thanks to Corey, Curtis, Calvin, and the staff at the JILA purchase order and admin offices. JILA has been an awesome place to work.

I must thank Professors Steven Pollock, András Gyenis, Adam Kaufman, and James Thompson who introduced me to a ton of exciting stuff in the land of quantum.

I would also like to thank my friends at CU who have made basically everything infinitely more fun (too many to name and I will invariably miss someone). I am very thankful to my mum, dad, and brother who have always supported me in every way possible.

Finally, I must thank COMSOL. We met during COVID and my life changed completely. However, things have not been not easy for us. At times, it has been an incredibly toxic relationship. I cannot count the number of times we have stayed up arguing until 2 AM. But COMSOL has always been there for me, and somehow, we managed to make things work in the end.

Contents

Chapter

Figures

Figure

Chapter 1

Introduction

1.1 Context

Highly tensioned mechanical resonators have been studied for several decades. They have been used in the context of exploring quantum science [2] – in experiments such as quantum transduction [1, 12, 25], creation of quantum memories [48, 18, 24], and squeezed light generation[30, 36, 6] – and for precision sensing applications – such as microscopy [16], magnetic force detection [35, 11], accelerometery [56], mass sensing, along with near-term proposals for quantum gravity experiments involving the detection of gravitational forces on small length scales [23, 39, 29].

In sensing applications employing a resonator mode, it is required to couple a resonator sensor to a quantity of interest. To acheive this coupling, it is often necessary to functionalize the resonator with a coupling agent. This results in an additional resonator mass. In certain applications such as magnetic force detection, gravitational force sensing, and accelerometry, the desired observable scales linearly with the added mass [43]. This can be written as $D = \beta M$, where D, β and M are the observable, quantity of interest and mass respectively. Typically, there is specific interest in the fundamental resonator mode since it is one where the mass always moves. The thermal Brownian force limited sensitivity to measure β in this mode is [19]

$$S_\beta = \sqrt{\frac{4k_BT\omega}{MQ}}, \tag{1.1}$$

where k_B, T, ω, M and Q are the Boltzmann constant, temperature, mechanical mode resonance frequency, added mass and mode quality factor, respectively. To optimize the sensitivity, we wish to minimize S_β. In general, a higher Q is more favourable for this purpose, however, a careful understanding of the dependence of Q on M is required [43].

Low optical absorption, high-stress obtainable in fabrication, along with other material properties make silicon nitride (SiN) a natural material for high Q resonator sensor design [57, 54, 41, 47]. In tensioned SiN resonator modes, typically, Q is limited by two loss mechanisms — bending loss, which is the energy lost due to the mode bending, and radiation loss, which is the energy lost from the mode into the surroundings via acoustic radiation. we define individual quality factors, $Q_{bending}$ and $Q_{radiation}$, associated with bending loss and radiation loss respectively, such that $\frac{1}{Q} = \frac{1}{Q_{bending}} + \frac{1}{Q_{radiation}}$. Over the years, multiple resonator engineering efforts have led to resonators with modes limited by bending loss where $Q \approx Q_{bending}$ [32, 46, 52, 49, 27, 50, 33, 5, 22, 14]. Thus, it is of interest to study the dependence of $Q_{bending}$ on M in highly tensioned mass-loaded SiN resonators.

1.2 Problem Statement

While there have numerous efforts to engineer ultrahigh Q SiN tensioned resonators for sensing, these have been limited to non-functionalized resonators [32, 46, 52, 49, 27, 50, 33, 5, 22, 14]. However, functionalization is crucial for sensing, and it involves appending a mass-carrying coupling agent to the resonator [43]. The added mass affects mode structure and $Q_{bending}$. Typically $Q_{bending}$ is drastically lowered thereby lowering the sensitivity. However, the exact dependence of $Q_{bending}$ on M has previously not been studied and there has been no work done to engineer ultrahigh $Q_{bending}$ in functionalized resonators. This thesis investigates the dependence of $Q_{bending}$ on M and provides some insight into engineering ultrahigh $Q_{bending}$ functionalized resonators.

1.3 Thesis Organization

Chapter 2 of this thesis discusses mechanical resonators as precision sensors. Specifically, I will discuss how a mechanical resonator can be modeled mathematically and introduce the mechanical susceptibility. Then, I will talk about thermal limited force sensitivity and introduce the mechanical quality factor Q. After that, I will pivot to resonator functionalization and mass loading. I will end by talking about the figure of merit for precision sensing and motivating the study of mass-loaded tensioned resonators. In particular, I will discuss why it is of interest to understand how mass loading a tensioned resonator affects the Q of its mechanical modes.

Chapter 3 of this thesis begins with a discussion of loss mechanisms in mechanical resonators since this ultimately decides Q. Then I move the special case of highly tensioned thin film silicon nitride mechanical resonators. After that, I outline recent efforts to improve the Q of highly tensioned thin-film silicon nitride mechanical resonators. I will end with a discussion of the current work in the field of mass-loaded tensioned resonators and outline the focus of the thesis.

Chapter 4 of this thesis discusses an ideal toy model of a highly tensioned mass-loaded string. We analytically study the effect of mass loading the string on the shape and Q of its fundamental modes. We show that in the limit of a large mass load, while the frequency continually decreases, the mode shape and Q both saturate.

Chapter 5 of this thesis outlines the experiment we performed to validate the theory-predicted Q saturation effect. In particular, I outline details of the resonator choice, mass loading protocol, and methods used to minimize radiation loss. I also discuss how the Q values were measured using a Fabry-Perot cavity with a ringdown measurement scheme, and talk about some technical details involving COMSOL FEM simulations of mechanical resonators. Finally, I discuss the experimental results which demonstrate Q saturation and talk about additional results which are relevant. Lastly, I talk about the implications of Q saturation for sensing.

Chapter 6 of this thesis is a conclusion chapter, and it outlines all the work done along with the results. It also outlines possible future work which might be of interest.

Chapter 2

Mechanical Resonators as Precision Sensors

2.1 Introduction to Mechanical Resonators

2.1.1 Equation of Motion for a Mechanical Resonator

A mechanical resonator is any object that can vibrate. Mechanical resonators are all around us – common daily life examples include guitar strings, drumheads, and tuning forks. More formally, if we ignore the trivial example of a single particle, a mechanical resonator can be defined as a multi-particle system with normal modes. A resonator normal mode is an oscillatory motion where every part of the resonator moves with the same frequency. Another way to picture normal modes is to think of them as standing waves. As indicated by their name, normal modes are mathematically orthogonal, and they form a basis to describe the motion of the resonator. Therefore, the general motion of a mechanical resonator can always be written as a linear combination of the motion of its individual normal modes along with a translation motion.

The normal modes of any mechanical system can be found by solving the relevant partial differential equation arising from the theory of elasticity while imposing appropriate boundary conditions [21]. Typically, the partial differential equation of interest tends to be a modified version of the wave equation. Fundamentally, this leads to an eigenvalue problem, and the solution yields a set of eigenvalues and eigenvectors. The eigenvalues are related to the mode angular frequencies ω_m, where m is the mode index, and $\omega_m = 2\pi f_m$ where f_m is the mode frequency. The normalized eigenvectors correspond to the mode displacement functions $u_m(\vec{r})$ where $\vec{r}$ is a position vector that refers to a specific point on the resonator, and $u_m(\vec{r})$ is the mode displacement function at that point.

Since we are interested in the motion of a resonator mode in time, the more relevant quantity to look at is the time-dependent mode displacement $u_m(\vec{r}, t)$ which is given by $u_m(\vec{r}, t) = x(t)u_m(\vec{r})$ where $x(t)$ is the time-dependent displacement. Assuming no driving force and damping, $x(t)$ would be a sinusoidal function oscillating at an angular frequency of ω_m. If damping is present, then we expect $|x(t)|$ to decrease with time, and in the underdamped regime, this is often modeled by multiplying a sinusoidal function oscillating at an angular frequency of ω_m with a decaying exponential. In general, the motion of an individual normal mode can be modeled using the driven-damped simple harmonic oscillator equation for $x(t)$:

$$\frac{d^2x(t)}{dt^2} + \Gamma_m \frac{dx(t)}{dt} + \omega_m^2 x(t) = \frac{F(t)}{m_{eff}}. \tag{2.1}$$

Here, Γ_m is the mechanical damping rate, $F(t)$ is the time-dependent external driving force, and m_{eff} is the effective mass of the mode. The mechanical damping rate Γ_m indicates the amount of damping present, and it is equal to the resonance linewidth of the mechanical mode. The effective mass m_{eff} is a quantity defined to be consistent with energy conservation. It allows us to treat the entire resonator mode as a single particle that is oscillating at an angular frequency ω_m, with displacement $x(t)u_m(\vec{r})$, and a mass equal to m_{eff}. See references [2, 11, 32] for a detailed discussion of the effective mass m_{eff}.

We can solve Equation (2.1) most easily in frequency space by using the Fourier Transform. For an arbitrary time-dependent function $g(t)$, the Fourier Transform gives the angular frequency dependent function $g(\omega)$ and is defined as follows:

$$g(\omega) = \int_{-\infty}^{\infty} g(t)e^{i\omega t}dt. \tag{2.2}$$

We can apply the Fourier Transform to both sides of Equation (2.1) and use standard properties of the Fourier Transform to simplify the resulting expression. This yields the following result:

$$-\omega^2 x(\omega) + i\Gamma_m \omega x(\omega) + \omega_m x(\omega) = \frac{F(\omega)}{m_{eff}}. \tag{2.3}$$

Thus, we obtain the expression for $x(\omega)$ as:

$$x(\omega) = \frac{F(\omega)}{m_{eff}(\omega_m^2 - \omega^2 + i\omega\Gamma_m)}. \tag{2.4}$$

Now, $x(t)$ can easily be found by computing the inverse Fourier Transform of $x(\omega)$:

$$x(t) = \int_{-\infty}^{\infty} \frac{1}{2\pi} x(\omega) e^{-i\omega t} dt. \tag{2.5}$$

In order to characterize the frequency response of our mechanical system, we define a complex-valued function called the mechanical susceptibility $\chi(\omega)$ as follows:

$$\chi(\omega) = \frac{x(\omega)}{F(\omega)}. \tag{2.6}$$

From Equation (2.4) we see that the mechanical susceptibility for our system is given by:

$$\chi(\omega) = \frac{1}{m_{eff}(\omega_m^2 - \omega^2 + i\omega\Gamma_m)}. \tag{2.7}$$

Fig. 2.1 shows $|\chi(\omega)|^2$ as a function of ω for a typical mechanical oscillator mode. Conceptually, the magnitude of the mechanical susceptibility tells us the steady-state displacement resulting from a unit magnitude sinusoidal driving force with angular frequency ω. Clearly, the magnitude of the susceptibility is a maximum when the driving angular frequency ω is equal to the mode angular frequency ω_m. This is characteristic resonance behavior. We note that the mechanical susceptibility is complex-valued in general because the mechanical response of the oscillator is not always in phase with the drive. The phase difference between the drive and the response is related to the ratio between the real and imaginary parts of the mechanical susceptibility. From Fig. 2.1, as mentioned earlier, we can see that the damping rate Γ_m is the resonance linewidth (full width half maximum).

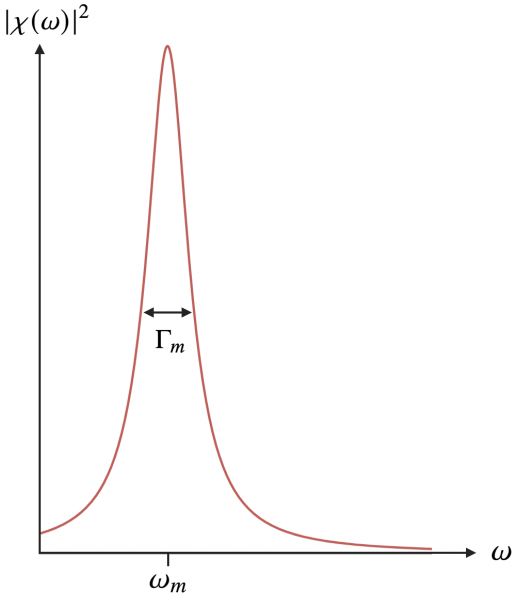

Figure 2.1: **Susceptibility Squared vs Driving Frequency.**

A plot of the magnitude squared of the mechanical susceptibility $|\chi(\omega)|^2$ versus the driving angular frequency ω for an underdamped resonator with mode angular frequency ω_m. In the underdamped regime, the damping rate Γ_m is assumed to be small compared to ω_m.

2.1.2 Force Sensitivity of a Mechanical Resonator

Now that we have covered the basic mathematical formulation behind mechanical resonators, we will focus on understanding how the normal modes of these devices can be used for sensing. Many sensing protocols rely on force detection of some sort [35, 11, 19, 56]

Thus, we wish to understand how the normal modes of mechanical resonators can be used to detect forces. Going back to Equation (2.1), we can see that when there is no external drive, $F(t) = 0$, we expect the oscillations of the resonator should decay to zero and thus, the steady-state solution should be $x_{ss}(t) = 0$. However, in practice, this never occurs. A resonator with a non-zero temperature is constantly interacting with a thermal bath, and due to the presence of the thermal Langevin force, $F_{th}(t)$, which arises from Brownian motion [2] in this bath, the resonator is constantly being "kicked" around. Therefore, the motion of the resonator under this thermal force, which is known as the thermal motion, $x_{th}(t)$, is non-zero in general. The thermal Langevin force, $F_{th}(t)$, is a random time-varying force whose average magnitude depends on the temperature of the resonator's thermodynamic bath [2]. Since $F_{th}(t)$ is random, it has a signed mean of zero.

When detecting a force with a resonator mode, we need to be able to distinguish between the motional response of the resonator which arises due to the force of interest from the response caused by the thermal force. In other words, the force sensitivity of a resonator mode is limited by the effect of the thermal force on the mode motion, and $F_{th}(t)$ sets the noise floor for force detection. We will now try to derive a mathematical expression for the force sensitivity of a resonator mode.

In experiments, instead of analyzing the motion $x(t)$ of a resonator in the time domain, we often look at the motion $x(\omega)$ in frequency space since this allows for the separation of the contribution from different modes. In particular, we look at the motion noise power spectral density which is loosely defined as:

$$S_{xx}(\omega) =< |x(\omega)|^2 > . \tag{2.8}$$

Overall, $S_{xx}(\omega)$ tells us about the motion of the resonator in frequency space squared, averaged over multiple experimental runs. Now, plugging in Equation 2.6 into Equation 2.8, we obtain:

$$S_{FF}(\omega) =< |F(\omega)|^2 >= \frac{S_{xx}(\omega)}{|\chi(\omega)|^2}. \tag{2.9}$$

This relates the force noise power spectral density to the motion noise power spectral density. Assuming thermal equilibrium, we can invoke the fluctuation-dissipation theorem [2] which connects the noise to the dissipation:

$$S_{xx}(\omega) = \frac{2k_bT}{\omega} \cdot Im[\chi(\omega)]. \tag{2.10}$$

Using Equation 2.10 and Equation 2.9, we obtain an important result:

$$S_{FF}(\omega) = 4k_bTm_{eff}\Gamma_m. \tag{2.11}$$

Here, k_b is the Boltzmann constant, and T is the resonator's temperature. As a note to the reader, there may be some incorrect factors of 2 and π floating around due to the different conventions used when defining Fourier transforms (see [2] for additional details).

The force noise power spectral density quantifies the force sensitivity of a resonator mode. The numerical value of S_{FF} tells us the size of the smallest force we can measure or resolve using our resonator mode if we average the motional power for unit time. As we can see, the smaller the value of S_{FF}, the better our resonator is for force sensing. From the above expression, we can see that there are three ways to improve the force sensitivity: lower the temperature T, lower the mode effective mass m_{eff}, or lower the damping rate Γ_m. The temperature T can be lowered by cryogenic cooling, and further, also by laser cooling mechanical modes through feedback damping or sideband cooling [2]. The effective mass m_{eff} is frequently lowered by carefully engineering the geometry of resonators, however, many sensing applications require appending a mass-carrying coupling agent to the resonator, and this unavoidably increases m_{eff}. Moreover, as will be discussed later, in some sensing applications, it is beneficial to use a large mass coupling agent. The damping rate Γ_m can be lowered through a variety of methods, and this will be the focus of the discussion for the rest of the paper. However, we will first need to understand the importance of a quantity known as the quality factor Q of resonator modes since this quantity is closely related to the damping rate Γ_m.

2.1.3 The Quality Factor (Q) of a Resonator Mode

As discussed in the previous section, a resonator mode that is undergoing free oscillations can be modeled as a damped harmonic oscillator [45]. When the damping is non-zero, as the resonator mode oscillates, it continuously loses energy, and as a result, the amplitude of oscillations decreases. In the underdamped regime where Γ_m is small, the amplitude of the oscillations decays exponentially [45]. Fig. 2.2 shows how the displacement $x(t)$ of an underdamped oscillator with initial amplitude A varies with time t. The envelope shows how the amplitude of the oscillations dies out exponentially.

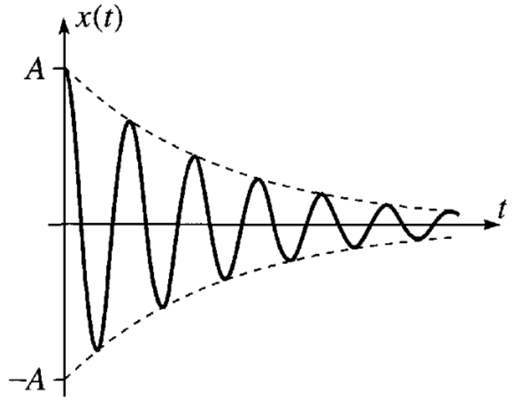

Figure 2.2: **Displacement of a Harmonic oscillator vs Time.**

Plot of the displacement $x(t)$ of an underdamped harmonic oscillator with initial amplitude A as a function of time t (solid black line). The amplitude of the oscillations dies out exponentially (dotted black line). This figure is adapted from [45].

One way to quantify the energy decay of a freely oscillating underdamped resonator mode is through the mode quality factor Q which is defined as:

$$Q = 2\pi \frac{W}{\Delta W}. \tag{2.12}$$

Here, W is the energy stored in the mode, and ΔW is the energy loss per oscillatory cycle. Mathematically, Q/π is roughly equal to the number of resonator mode oscillations that occur before the mode amplitude decreases by a factor e. Thus, qualitatively, Q is a measure of the number of coherent mode oscillations that can occur before a significant amount of energy is lost from the mode to the environment. In the underdamped regime where Γ_m is small, we can approximate Q by:

$$Q \approx \frac{\omega_m}{\Gamma_m}. \tag{2.13}$$

Here, ω_m mode angular frequency and Γ_m is the damping rate. As visible, this relation tells us that the smaller the damping rate Γ_m, the larger the Q and the narrower the resonance linewidth.

Since it is connected to Γ_m, Q is an important figure of merit in precision sensing and quantum science applications that use a mechanical mode. As explained in the previous section, many precision sensing applications using a mechanical resonator rely on force detection. Qualitatively, a higher Q is better for this purpose because it means that the resonator is better at retaining information about an external force or perturbation. Mathematically, this can be seen from Equation (2.11) which can be rewritten in terms of Q as follows:

$$S_{FF} = \frac{4k_bTm_{eff}\omega_m}{Q}. \tag{2.14}$$

Clearly, a higher Q simply leads to better force sensitivity, and this is beneficial for numerous sensing protocols relying on force detection [35, 11, 19, 56]. As an aside, a higher Q also means the mode frequency is more well-defined due to the narrow linewidth, and this is helpful for sensing applications that rely on accurate measurements of frequency shifts [51, 8, 20]. Thus, high Q is of utmost importance for sensing in multiple contexts. In the next subsection, we take a closer look at how the force sensitivity applies directly to precision sensing applications.

2.2 Precision Sensing with Mechanical Resonators

2.2.1 Resonator Functionalization and Mass Loading

Mechanical resonators have been studied for many decades for numerous precision sensing protocols. They have been used for applications such as magnetic force detection [35, 11] and accelerometer design [19, 56]. Recently, they have been proposed for studying gravitational forces on small length scales to test different models of quantum gravity [23, 39]. In all these applications, it is necessary to couple the physical quantity which is to be measured to the mechanical motion of the resonator. This is often (but not always) achieved through resonator functionalization which involves appending a coupling agent to the resonator (Fig. 2.3). An interaction between the physical quantity to be measured and the coupling agent results in a force that drives the mechanical resonator. The motion can be detected and used to indirectly measure the physical quantity.

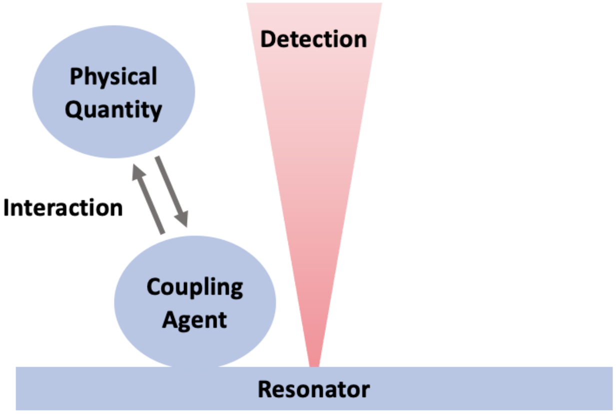

Figure 2.3: **Precision Sensing using a Mechanical Resonator.**

A mechanical resonator is functionalized with a coupling agent. The coupling agent mediates an interaction between the physical quantity to be measured and the resonator which results in a force that drives the resonator. The resulting resonator motion can be detected and used to indirectly measure the physical quantity.

As a specific example, for magnetic force detection from a sample of spins in the solid state, one could append a magnetic particle to the resonator to help mediate an interaction between the resonator and the spins. This would result in a force, when the spins are precessing for example, and cause resonator motion which can be read out optically. Similar schemes have been used to detect a single electron spin [35] as well as an ensemble of spins [11] using functionalized mechanical resonators.

Resonator functionalization involves appending a coupling agent to the resonator, and this unavoidably results in additional local mass on the resonator. This added mass can have a variety of different effects. If we look at a specific mode, we note the added mass can (a) lower the mode frequency ω_m, (b) change the effective mode mass m_{eff}, and (c) affect the mode quality factor Q. Thus, the added mass affects the force sensitivity S_{FF}, and it is therefore important to understand the details of exactly how this happens since this will ultimately affect the sensing capability of the resonator. As a note, we mainly focus on the fundamental mode of the resonator as in this mode the coupling agent is guaranteed to move and therefore it can effectively be used to drive the mode.

2.2.2 Figure of Merit for Precision Sensing

In this section, we will look more carefully into how a mass load that comes from adding a coupling agent affects the force sensitivity S_{FF}. We first note that in some applications, the desired observable scales with the added mass, explicitly $D = \beta M$, where D, β, and M are the observable, quantity of interest, and mass respectively. Examples include magnetic force sensing [35, 11], accelerometry [19, 56] and detection of gravitational forces [23, 39, 29]. Thus there is an immediate reason to simply use a larger mass coupling agent. However, we need to carefully analyze how this affects S_{FF}. Specifically, we define $S_\beta = \frac{\sqrt{S_{FF}}}{M}$ which gives us the fundamental sensitivity for measuring β (assuming the sensitivity is limited by thermal force noise). We first note that for a large mass coupling agent, $m_{eff} \approx M$, that is the effective mode mass is approximately equal to the coupling agent mass. We can model our mechanical resonator mode as a simple harmonic oscillator with an effective spring constant k, and then we know $\omega_m = \sqrt{\frac{k}{M}}$. Note that k is generally not a function of M. Under these conditions, S_β is given by:

$$S_\beta = \sqrt{\frac{4k_bTk^{\frac{1}{2}}}{M^{\frac{3}{2}}Q}}. \tag{2.15}$$

2.2.3 Motivation to Study Mass Loaded Mechanical Resonators

From Equation(2.15), it appears that the fundamental sensitivity can be improved by simply increasing M. However, we must be aware that in general since adding a local mass load to a resonator can affect its mode Q, in general, Q is a function of M. Typically, added mass tends to lower the Q [11]. Thus, it is important to understand how Q depends on M since this will allow us to quantify precisely how the fundamental sensitivity S_β scales with M. In this thesis, I will discuss the problem of the effect of a local mass load on a mechanical resonator. In particular, I will focus on how the added mass affects the Q of a resonator's mechanical modes. Since Q is ultimately linked to energy loss in a mechanical resonator, I will carefully discuss the sources of energy loss in a mechanical resonator and use this as a tool to study the effect of mass loading on Q. For reasons outlined in the next section, I will restrict my attention to highly tensioned thin film silicon nitride mechanical resonators.

Chapter 3

Tensioned Silicon Nitride Mechanical Resonators

3.1 Loss Mechanisms in Mechanical Resonators

3.1.1 Overview of Loss Channels

Energy loss due to damping in mechanical resonators can be divided into two broad categories – internal loss and external loss. We indicate this by writing the total energy loss per cycle as $\Delta W = \Delta W_{internal} + \Delta W_{external}$, thereby separating the internal and external loss contributions respectively. We define the internal loss $\Delta W_{internal}$ as the amount of the mode's mechanical energy that is converted to heat, and the external loss $\Delta W_{external}$ as the amount of the mode's energy escaping from the resonator to its environment. Using the definition of mechanical quality factor as given in Equation (2.12) we can divide the quality factor into its internal and external components:

$$Q = (Q_{internal}^{-1} + Q_{external}^{-1})^{-1} \tag{3.1}$$

From this equation, we see that Q can be improved by increasing $Q_{internal}$ or $Q_{external}$ or both. In order to be able to do this, we first need to obtain an in-depth understanding of the reasons for internal loss $\Delta W_{internal}$ and external loss $\Delta W_{external}$. Generally, both $\Delta W_{internal}$ and $\Delta W_{external}$ are each composed of multiple loss mechanisms [38]. In each case, the dominant loss mechanism depends on the type of mechanical resonator that is being dealt with. I will restrict my attention to mechanical resonators made from thin-films of highly tensioned material. Specifically, I will focus on the out-of-plane mechanical modes of such resonators and analyze the loss mechanisms when the displacement amplitude is small and the experimental conditions are ideal.

3.1.2 Internal Losses

Internal loss is defined as mechanical energy in the resonator mode that is converted to heat. Common internal loss channels include thermoelastic damping loss, surface loss, two-level defect loss, and material bending loss. In the out-of-plane mechanical modes of highly tensioned thin-film resonators, internal loss is dominated by material bending loss which we denote by $\Delta W_{bending}$. Therefore, for this class of resonators $\Delta W_{internal} \approx \Delta W_{bending}$, and therefore, $Q_{internal} \approx Q_{bending}$. Simply put, material bending loss is the energy loss associated with the bending of the resonator as it oscillates. Typically, materials are not purely crystalline and there are structural imperfections in the form of defects. Due to the presence of these defects, as the material bends, energy is lost. The precise mechanism of energy loss in these defects is extremely complicated [38] and beyond the scope of this work. Importantly, material bending loss is a function of the mode shape of the resonator. We can now try to obtain a mathematical formula for $Q_{bending}$.

Consider a planar resonator with the out-of-plane mode displacement function $u(x, y)$ where x and y are the in-plane resonator coordinates. Since the resonator is made from a thin-film, the thickness h of the resonator is assumed to be much smaller than the in-plane resonator dimensions. Further, since the displacement amplitude is small, we expect $|u(x, y)| \ll h$. Finally, since the resonator has a highly in-plane tension, we can translate this to a large in-plane tensile stress denoted by σ. Under these assumption, it can be shown that $\Delta W_{bending}$ is approximated by:

$$\Delta W_{bending} \approx \int_V \frac{\pi E_2}{1-\nu^2} z^2 \left(\frac{\partial^2 u(x,y)}{\partial x^2} + \frac{\partial^2 u(x,y)}{\partial y^2} \right)^2 dV. \tag{3.2}$$

The term in parentheses in Equation (3.2), $\left(\frac{\partial^2 u(x,y)}{\partial x^2} + \frac{\partial^2 u(x,y)}{\partial y^2} \right)$, is the mean curvature, and the volume integral of this quantity over the resonator volume essentially decides $\Delta W_{bending}$. From this, we can conclude that regions of the resonator that bend more and have higher curvature contribute more to the energy loss. This is an important conclusion which will be used later in this thesis. Next, we can approximate the stored tensile energy W as:

$$W \approx \int_V \frac{\sigma}{2} \left(\left(\frac{\partial u(x,y)}{\partial x} \right)^2 + \left(\frac{\partial u(x,y)}{\partial y} \right)^2 \right) dV. \tag{3.3}$$

In these equations, E_2 is the imaginary part of the resonator material's complex-valued Young's modulus, ν is its Poisson ratio, z is the resonator's coordinate along its thickness, and V is the volume of the resonator. Applying Equation (2.12) we can see that $Q_{bending}$ is given by:

$$Q_{bending} \approx \left(\frac{\int_V \sigma \left(\left(\frac{\partial u(x,y)}{\partial x} \right)^2 + \left(\frac{\partial u(x,y)}{\partial y} \right)^2 \right) dV}{\int_V \left(\frac{E_2}{1-\nu^2} \right) z^2 \left(\frac{\partial^2 u(x,y)}{\partial x^2} + \frac{\partial^2 u(x,y)}{\partial y^2} \right)^2 dV} \right). \tag{3.4}$$

This is a very messy equation, but the key thing to notice is that, for a given resonator mode, $Q_{bending}$ is purely a function of the mode displacement function $u(x, y)$. In other words, we can easily see that $Q_{bending} = Q_{bending}(u(x, y))$. This implies that the mode displacement function or mode shape decides $Q_{bending}$.

3.1.3 External Losses

External loss is defined as the energy lost from the resonator mode to its environment. Common external loss channels are radiation loss and gas damping. Typically, working in high-vacuum environments eliminates gas damping for thin-film mechanical resonators with a relatively small surface area. Therefore, the dominant external loss channel is radiation loss and this implies $\Delta W_{external} \approx \Delta W_{radiation}$ and $Q_{external} \approx Q_{radiation}$. There are two different ways to model radiation loss. In the first, radiation loss is simply the loss of energy from a mechanical mode due to the mode sending disturbances or acoustic waves into the surroundings. These waves never return, so effectively, the resonator has lost energy. In the second, we can think of radiation loss in term of mode hybridization which describes the coupling between normal modes of the resonator and its surrounding environment. Radiation loss can be thought of the energy lost due to this coupling. Simply put, as the resonator mode oscillates, due to mode hybridization, energy leaks from the resonator mode into modes of the environment and is therefore lost.

Radiation loss is most pronounced in lower order resonator modes such as the fundamental resonator mode. It is significantly lower in higher order antisymmetric modes where the center of mass of the resonator does not move. This is because, in higher order antisymmetric modes, the acoustic radiation pattern in the external substrate leads to destructive interference (due to symmetric cancellation) and effectively lowers the net amount of acoustic wave radiation. Radiation loss is also strongly affected by how a resonator is physically mounted [34, 50, 27, 33]. Typically, placing a resonator under its own weight leads to the highest Q values. Rigidly clamping or holding a resonator can lower Q by many orders of magnitude [50]. Overall, radiation loss is a complex phenomenon which has been historically difficult to model and understand. There is no single well-known mathematical expression for radiation loss that fits the different scenarios which appear in experiments.

3.1.4 Combining Internal and External Loss

In the previous two subsections, we discussed the dominant internal and external loss mechanisms in highly tensioned planar thin-film mechanical resonators. We concluded that for this class of resonators, $Q_{internal} \approx Q_{bending}$ and $Q_{external} \approx Q_{radiation}$. Based on Equation (3.1), we can conclude that:

$$Q = (Q_{bending}^{-1} + Q_{radiation}^{-1})^{-1} \tag{3.5}$$

This is a very important equation and I will refer to it frequently. Now that we have understood how the Q of a resonator mode is affected by the different energy loss channels, we can move to study how higher Q mechanical modes can be engineered. However, before we do that, we need to discuss the specific case of SiN mechanical resonators.

3.2 Tensioned Silicon Nitride Mechanical Resonators

3.2.1 Tensioned Silicon Nitride

Tension Silicon Nitride (SiN) is frequently used to make mechanical resonators due to its favorable optical and mechanical properties [57].

SiN is partially reflective and this allows for the detection of mechanical mode motion through laser interferometry, often using a Michelson interferometer or a Fabry-Perot interferometer. Further, this partial reflectivity is crucial for optomechanics experiments that rely on backaction [2]. SiN also has low optical absorption which enables mode motion to be detected without significant heating [57]. This is also important for applications that require mechanical resonators to be at extremely low temperatures.

Highly tensioned thin-films of SiN can be grown chemically. Such films are of interest because high tension leads to a phenomenon known as dissipation dilution which results in increased Q [10]. Further, tension allows us to access very high frequencies without shrinking the device size. High tension has enabled millimeter-scale SiN membranes to have mode frequencies in the MHz range. This is invaluable as it allows for convenient optical detection to be maintained while going to higher frequencies. It is often useful to work at high frequency as $1/f$ noise is lower and some applications require high frequency [2].

Devices made from thin-films have modes with lower effective masses which is beneficial for applications such as force sensing [32]. Thin films are also of interest, because bulk losses can be ignored, allowing the possibility of higher Q modes dominated by surface loss [46].

Finally, it is worth mentioning that typically, stoichiometric SiN with the chemical formula Si_3N_4 is used, and resonators are made through standard cleanroom micro-fabrication. There are well-established micro-fabrication techniques that allow SiN to be patterned, and this is crucial to make devices with ultra high Q modes.

3.2.2 $Q_{bending}$ for High Stress Thin Film Silicon Nitride Resonators

Looking back at Equation (3.2), we see the imaginary part of the material's complex Young's modulus, E_2, in the integrand. In general, for thin-films of SiN, E_2 is a function of z, which is the coordinate along the resonator's thickness axis [46]. In particular, the surface value of E_2 is much higher than the bulk value. This implies that most of the loss ΔW is due to loss at the surface of the material [46]. As a result, if we assume a thin lossy layer at either surface of the resonator, the volume integral in Equation (3.2) can be reduced to a surface integral. Thus, $Q_{bending}$ as given in Equation (3.4) reduces to:

$$Q_{bending} = \frac{24(1-\nu^2)(Q_{intrinsic}(h))W}{Eh^3}\int_S\left(\frac{\partial^2 u(x,y)}{\partial x^2}+\frac{\partial^2 u(x,y)}{\partial y^2}\right)dS. \tag{3.6}$$

Here, W is the same as in Equation (3.3), E is the Young's modulus, h is the resonator thickness, S is the surface of the resonator, and finally, $Q_{intrinsic}(h)$ is the thickness dependent intrinsic quality factor. $Q_{intrinsic}$ is a measure of how lossy the material is, and the higher the value of $Q_{intrinsic}$, the less lossy the resonator material is. Further, $Q_{intrinsic}$ sets an upper bound on $Q_{bending}$. For SiN in particular, $Q_{intrinsic} \propto h$ and we have that $Q_{intrinsic} = E/E_2$. For reference, 100 nm thick SiN has $Q_{intrinsic} \approx 6000$ at a temperature of 300 K. The value of $Q_{intrinsic}$ increases for SiN as we cool down to cryogenic temperatures and is roughly 3 times larger at a temperature of 4 K as compared to 300 K. The key thing to take away from Equation (3.6) is that $Q_{bending}$ is essentially decided by the surface integral of the mean curvature over the mode shape. As a reminder, the mean curvature is given by: $\left(\frac{\partial^2 u(x,y)}{\partial x^2}+\frac{\partial^2 u(x,y)}{\partial y^2}\right)$. This is a very important conclusion as it essentially tells us that $Q_{bending}$ is limited by regions of the mode exhibiting high curvature, and therefore, reducing high curvature is key to improving $Q_{bending}$. As a note to the reader, deriving Equation 3.6 from Equation 3.4 is somewhat complicated [46, 32].

3.2.3 A General Formula for $Q_{bending}$

We note that Equation 3.6 is a special case of a general result from the theory of elasticity [21]. In general, can write the $Q_{bending}$ contribution from some physical domain as:

$$Q_{bending} = \left(\frac{2Q_{intrinsic}}{E}\right)\frac{W}{\int_{epoxy}\left(\sum_{ij}(\epsilon_{ij})^2\right)dV} \tag{3.7}$$

This formula is especially useful when studying mass loading because the resonator now has an additional local mass appended to it, often with some form of epoxy, and it becomes crucial to calculate the bending loss inside the epoxy. This is because the loss in the epoxy often turns out to be dominant [43]. The above formula does not assume high-stress or dominant surface loss [21].

Further, it includes mechanical loss due to three-dimensional deformation. However, it does assume a spatially uniform intrinsic quality factor.

3.3 Methods to Improve Q in Silicon Nitride Resonators

So far, we have rigorously analyzed the relevant loss mechanism for highly tensioned thin-film SiN mechanical resonators. I will now discuss the variety of ways in which SiN resonators have been engineered to produce modes with ultra-high Q. I will refer to are Equations (2.12), (3.5) ,and (3.6) which are key to understand the basis of these techniques. Looking at the definition of Q as given in Equation (2.12), it is clear that the Q of a resonator mode can be improved by either increasing the energy W of the mode or lowering the energy loss per cycle ΔW. In this section I will review methods which both use these approaches to improve Q.

3.3.1 Dissipation Dilution

3.3.1.1 High Stress Suspensions

The Q of a resonator mode can be improved by increasing the energy W of the mode without a similar increase in the loss per cycle ΔW. From Equation (3.3), we see that this can be achieved by increasing the film-stress σ. This technique is known as dissipation dilution and it is a direct method to improve the Q of modes [10]. Since SiN can be grown with a tunable film-stress σ, this is a natural way to create resonators with high Q modes. SiN has a yield stress of $\sigma_{yield} = 7\ GPa$ and it is common for resonators to be made from films with stresses as high as $\sigma = 1\ GPa$ [57]. This technique has allowed for devices such as membranes to have mode Q values as high as 10^8 [54] at cryogenic temperatures.

3.3.2 Mode Shape Engineering

A different way to improve the Q of a resonator mode is to decrease the energy loss per cycle ΔW. We recall that $\Delta W = \Delta W_{bending} + \Delta W_{radiation}$. Mode shape engineering is a widely used technique to improve Q and it relies on lowering $\Delta W_{bending}$. To understand the fundamental guiding principle behind mode shape engineering, we can study the mode profile of a square membrane mode. Fig. 3.1 shows how the mean curvature of a square membrane mode varies along a line-cut across the mode. In particular we have the (2,2) mode of a square membrane which is clamped on all 4 sides. The dotted black line shows the line-cut, and the solid black curve is the mean curvature evaluated on this line-cut.

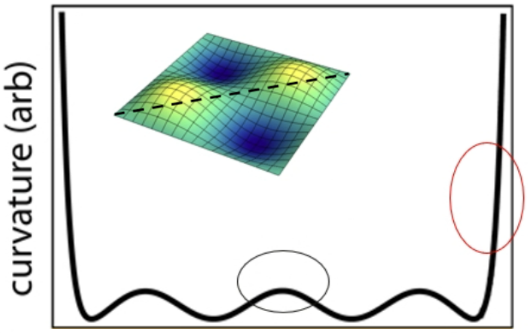

Figure 3.1: **Curvature Along Diagonal Line Cut for 2,2 Mode of a Membrane.** Plot of the curvature (solid black curve) evaluated on a line-cut (dotted line on inset) on the (2,2) mode of a square membrane (see inset) which is clamped on all 4 sides. The curvature is significantly larger at the mode edges due to the clamped boundary conditions.

We notice that the curvature is significantly larger at the mode edges due to the clamped boundary conditions. In fact it turns out that in this scenario $\Delta W_{bending}$ is completely dominated by curvature at the mode edges. This motivates resonator designs which try to alleviate this high curvature at the mode edge by patterning the resonator. I will now review some of these designs and explain how they work.

3.3.2.1 Trampoline Resonators

To minimize the effects of clamping on the curvature at the mode edges in membranes, these devices can be efficiently patterned. This has been done in multiple groups across the world to create trampoline resonators [34, 26]. Fig. 3.2 shows a microscope image of a SiN trampoline resonator. Compared to membranes, a lot of the SiN has been removed in trampolines. The device consists of a central pad suspended by 4 narrow tethers. The pad allows for convenient optical readout. At the corners where the tethers connect to the frame of the device, fileting is used to lower clamping losses. Filets help re-distribute the stress near the edges of the mode and nearly eliminate the kink in the mode shape. Thus the high curvature region is no longer present near the mode edges. As a result, compared to membranes at the same frequency, trampolines have much higher Q. These devices have measured Q values close to 10^9 and have shown quantum coherent oscillations at room temperature [34, 26, 17].

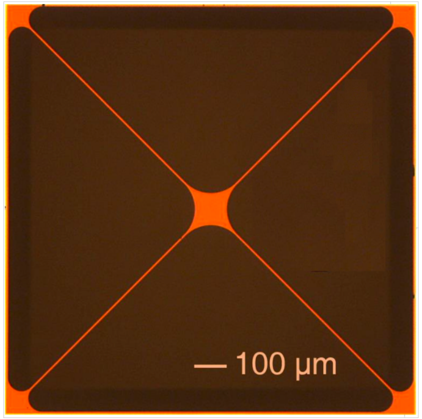

Figure 3.2: **Microscope Image of a Trampoline Resonator.**

A microscope image of a silicon nitride trampoline resonator (shown in orange). The trampoline consists of a central pad for optical detection which is suspended by four tethers. The tethers connect to the frame of the resonator via filets, which help reduce clamping losses. This figure is adapted from [43, 42].

3.3.2.2 Soft Clamped Resonators

Another form of mode shape engineering involves a technique known as soft-clamping. As discussed previously, typically, at the boundary of resonators such as membranes, due to clamped boundary conditions, bending loss is enhanced. A way to lower this bending loss is to employ soft clamping. In the 3.3, we can see a patterned resonator (on the left) which is known as a phononic crystal (PnC) [46, 32]. At the center of the PnC, we can see the presence of a defect, and this is because the central region breaks the crystalline pattern. Looking closely at the crystal bulk, we see that each unit cell is composed of a pad surrounded by tethers. In general, the stress, and hence the speed of sound in the tethers is higher as compared to the pad. Thus, as we move across the crystal, the speed of sound alternates between high and low. By Bragg scattering theory, this leads to the formation of an acoustic bandgap – a range of frequencies where mechanical disturbances cannot pass through the crystal structure [32]. Thus, the crystal structure has no mechanical modes at these frequencies. However, the central defect is designed such that it has modes with frequencies within the acoustic bandgap of the crystal. Thus, the motion of the defect can in essence be "trapped" within the crystal.

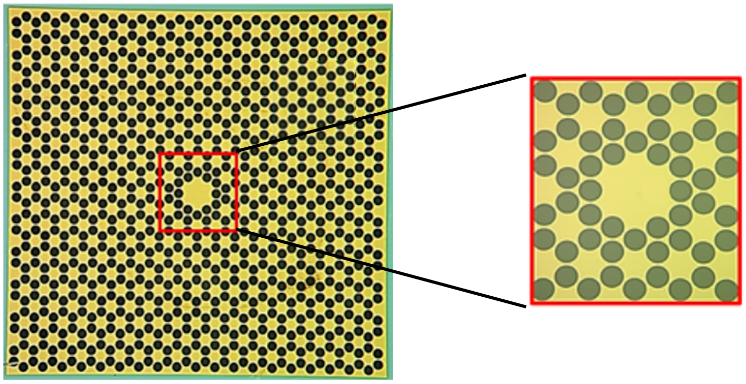

Figure 3.3: **Silicon Nitride Phononic Crystal with Defect.**
An image of phononic crystal with a defect (left). The soft-clamped defect (right) shows how the crystal pattern is broken to help create a spatially isolated mode. This figure is adapted from [32].

The result of this is design soft clamping. We can think of the defect as our resonator of interest. Unlike a standard membrane, the edges of the defect are not rigidly clamped since they simply attach to the crystal which is free to move. However, due to the acoustic bandgap, the motion of the defect decays evanescently into the crystal. If there are enough crystal unit cells, the defect mode motion decays enough such that, by the time the end of crystal structure is reached, the motion is so low that the clamped boundary conditions at the resonator edge do not influence bending loss. This ensures that the overall bending loss is minimized. This is visualized from the defect mode shape in Fig. 3.3 (on the right) where the mode displacement decays exponentially into the surrounding crystal. PnCs with defects have been pioneered by multiple mechanics groups across the world [46, 32], and they have allowed access to ultra-high Q mechanical modes which are of interest for sensing.

3.3.3 Acoustic Isolation

While mode shape engineering is one method to improve the Q of resonator modes, other methods exist. In particular, acoustic isolation is a well-known technique to improve $Q_{radiation}$ which is the Q associated with radiation loss. Lowering radiation loss is one avenue to improve the Q of resonator modes.

3.3.3.1 Mounting

The method by which resonators are physically mounted can significantly affect their mode quality factors due to radiation loss. This is especially true for the fundamental mode and other lower-order symmetric modes. Antisymmetric modes are somewhat “protected” against radiation loss. Membranes are especially susceptible to radiation loss. There are certain techniques to mount mechanical resonators to minimize radiation loss [50, 27, 33]. Typically, rigidly holding/fixing a resonator in any way can significantly lower the mode quality factor due to radiation loss. In general, it is widely accepted within the mechanics community that placing resonators under their own weight is the best way to minimize radiation loss. However, this area of research has almost no concrete work that has been published. In Sec. (5.1.3) of this thesis, we highlight some new work on mounting trampolines.

3.3.3.2 Phononic Crystal Defects

An example of an acoustically isolated resonator is a PnC with a defect, which we discussed earlier in the context of soft clamping. A PnC contains an acoustic bandgap, and as a consequence, a defect mode in the bandgap has lower radiation loss than a mode outside the bandgap [46, 32]. This can be understood qualitatively using a simple picture. We can think of an oscillating mode as a source of acoustic waves. When a defect mode is in the bandgap of a PnC, the acoustic waves it radiates are not allowed to propagate through the PnC. This is because the PnC contains no modes at the bandgap frequencies. Thus an in-bandgap defect mode is acoustically isolated and has lower radiation loss. Moreover, these types of modes are robust to mounting, and the Q does not depend on how the device is mounted. Acoustically isolated in-bandgap defect modes in a PnC have been shown to have ultra-high Q [46, 32].

3.4 Mass Loading and $Q_{bending}$

In the previous chapter, we saw why it is important to study the effect of mass loading on the Q of a resonator for precision sensing applications. In this chapter, we took a closer look at what decided the Q of a mechanical resonator. In particular, we narrowed down to high-stress thin film SiN membranes and studied the different approaches that have been taken to improve the Q of mechanical resonator modes. However, this was entirely for resonators without a mass load. Experiments have shown, although essential for sensing, that mass loading typically lowers the Q by enhancing the local curvature significantly, which in turn lowers the sensitivity. Little to no work has been done on the effect of Q on mass loading, and further, on optimizing the Q of mass-loaded resonators. As outlined in this chapter here are methods by which radiation loss can be lowered to enter a regime where $Q \approx Q_{bending}$, thus, what we really care about is how $Q_{bending}$ is affected by mass loading. The rest of this thesis will focus on exactly this question.

Chapter 4

Theoretical Analysis of Mass Loaded Mechanical Resonators

4.0.1 Mass Loaded String

To gain insight into how the shape and $Q_{bending}$ of the mechanical modes of a resonator are affected by mass loading, we begin by studying the simplest possible scenario that can be dealt with analytically – a mass loaded string [43]. Consider a string of length L, thickness h, and width w (Fig 4.1(a)). Let the spatial coordinate along the string's length be x where $0 \leq x \leq L$. Further, let the string's density vary along its length and be denoted by $\rho(x)$. We can define the value of $\rho(x)$ to be equal to ρ_m in the unloaded regions ($0 \leq x < a$ and $b < x \leq L$ for $a < b$), and equal to $\rho_m + \rho_M$ in the mass loaded region ($a \leq x \leq b$). Notice if $\rho_M = 0$ then we are simply looking at a string without a mass load and total unloaded resonator mass is $M_{unloaded} = hwL\rho_m$. However, if $\rho_M > 0$ then the string has an added mass $M_{load} = hw(b-a)\rho_M$ which is equally distributed over the region where $a \leq x \leq b$. Thus, by varying the value of ρ_M, we can emulate a mass load. Finally, let the string be doubly clamped, have a Young's Modulus E, and an in-plane tensile stress equal to σ_0.

We can study the modes of the string and begin to understand how the mode shape and $Q_{bending}$ change as we vary the mass load M_{load}. For simplicity, we stick to analyzing the fundamental out-of-plane mode of the string, however, the same analysis will apply to other out-of-plane modes. We denote the mode displacement function by $u(x)$. The equation governing the string's behavior is given by the stressed Euler-Bernoulli beam equation [38]

$$\frac{Eh^2}{12\sigma_0}\frac{d^4u(x)}{dx^4} - \frac{d^2u(x)}{dx^2} - \frac{\rho(x)(2\pi f)^2}{\sigma_0}u(x) = 0, \tag{4.1}$$

which is essentially a form of the wave-equation with an additional fourth derivative term to accurately capture the bending of the string's mode at the clamped edges. The width w is absent from the equation because the string is of uniform width. For clarification, the above equation is purely spatial, that is, the time dependence contained in the full partial differential equation has been removed by using the separation of variables technique. This is done because we are only interested in the mode shape. First, we will try to find the frequencies of the string's fundamental mode. If the in-plane tensile stress σ_0 is large and satisfies the length scale inequality $l = 2\pi\sqrt{\frac{Eh^2}{12\sigma_0}} \ll L$, then the fourth derivative term can be ignored when calculating the mode frequencies [38]. Thus, the string equation simplifies to

$$\frac{d^2u(x)}{dx^2} + K\left(x\right)^2 u = 0, \tag{4.2}$$

where we know that

$$K^2(x) = \begin{cases} \frac{\rho_m}{\sigma_0}\left(2\pi f\right)^2 & \text{for } 0 \leq x < a, \quad b < x \leq L \\ \frac{\rho_m+\rho_M}{\sigma_0}\left(2\pi f\right)^2 & \text{for } a \leq x \leq b \end{cases}. \tag{4.3}$$

Since the string is doubly clamped and the mass loaded region connects smoothly to the unloaded regions, the boundary conditions are

$$\text{BC:} \begin{cases} u(0) = u(L) = 0 \\ u(x) \text{ is continuous at } x = a, b \\ \frac{du(x)}{dx} \text{ is continuous at } x = a, b \end{cases}.$$

We notice that the general solution to Eq (4.2) in each of the three regions of the string is simply given by $A_{region} \cdot sin(\sqrt{K_{region}}x) + B_{region} \cdot cos(\sqrt{K_{region}}x)$ where A_{region} and B_{region} are arbitrary constants. We can now define the density ratio $\chi = \frac{\rho_M}{\rho_m}$ and introduce the mass loaded region wavenumber $\alpha = \frac{2\pi f}{v_{load}} = 2\pi f\sqrt{\frac{\rho_m+\rho_M}{\sigma_0}}$ where $v_{load} = \sqrt{\frac{\sigma_0}{\rho_m+\rho_M}}$ is the speed of sound in the mass loaded region of the string. Similarly, the wavenumber in the unloaded regions is $\beta = \frac{2\pi f}{v_{unloaded}} = 2\pi f\sqrt{\frac{\rho_m}{\sigma_0}}$ where $v_{unloaded} = \sqrt{\frac{\sigma_0}{\rho_m}}$ is the speed of sound in the unloaded regions of the string.

Using the first boundary condition along with trigonometric identities can help eliminate the cosine dependence in the unloaded regions, and it can be shown that

$$u(x) = \begin{cases} A_1 \sin\left(\frac{\alpha}{\sqrt{1+\chi}}x\right) & 0 \le x < a \\ A_2 \sin\left(\alpha\left(x - \frac{a+b}{2}\right)\right) + B_2 \cos\left(\alpha\left(x - \frac{a+b}{2}\right)\right) & a \le x \le b \\ A_3 \sin\left(\frac{\alpha}{\sqrt{1+\chi}}(L-x)\right) & b \le x < L \end{cases} \cdot \tag{4.4}$$

To find α, we write the remaining boundary conditions as a matrix vector equation in the unknown coefficients A_1, A_2, B_2, A_3:

$$\begin{pmatrix} \sin\left(\frac{\alpha}{\sqrt{1+\chi}}a\right) & -\sin\left(\alpha\left(\frac{a-b}{2}\right)\right) & -\cos\left(\alpha\left(\frac{a-b}{2}\right)\right) & 0 \\ \frac{\alpha}{\sqrt{1+\chi}}\cos\left(\frac{\alpha}{\sqrt{1+\chi}}a\right) & -\alpha\cos\left(\alpha\left(\frac{a-b}{2}\right)\right) & \alpha\sin\left(\alpha\left(\frac{a-b}{2}\right)\right) & 0 \\ 0 & \sin\left(\alpha\left(\frac{b-a}{2}\right)\right) & \cos\left(\alpha\left(\frac{b-a}{2}\right)\right) & -\sin\left(\frac{\alpha}{\sqrt{1+\chi}}(L-b)\right) \\ 0 & \alpha\cos\left(\alpha\left(\frac{b-a}{2}\right)\right) & -\alpha\sin\left(\alpha\left(\frac{b-a}{2}\right)\right) & \frac{\alpha}{\sqrt{1+\chi}}\cos\left(\frac{\alpha}{\sqrt{1+\chi}}(L-b)\right) \end{pmatrix} \begin{pmatrix} A_1 \\ A_2 \\ B_2 \\ A_3 \end{pmatrix} = \begin{pmatrix} 0 \\ 0 \\ 0 \\ 0 \end{pmatrix}. \tag{4.5}$$

Since there is more than one solution to Eq(4.5), the matrix on the left side must be non-invertible. Therefore, we can set its determinant equal to zero and obtain a transcendental equation for α:

$$\det\begin{pmatrix} \sin\left(\frac{\alpha}{\sqrt{1+\chi}}a\right) & -\sin\left(\alpha\left(\frac{a-b}{2}\right)\right) & -\cos\left(\alpha\left(\frac{a-b}{2}\right)\right) & 0 \\ \frac{\alpha}{\sqrt{1+\chi}}\cos\left(\frac{\alpha}{\sqrt{1+\chi}}a\right) & -\alpha\cos\left(\alpha\left(\frac{a-b}{2}\right)\right) & \alpha\sin\left(\alpha\left(\frac{a-b}{2}\right)\right) & 0 \\ 0 & \sin\left(\alpha\left(\frac{b-a}{2}\right)\right) & \cos\left(\alpha\left(\frac{b-a}{2}\right)\right) & -\sin\left(\frac{\alpha}{\sqrt{1+\chi}}(L-b)\right) \\ 0 & \alpha\cos\left(\alpha\left(\frac{b-a}{2}\right)\right) & -\alpha\sin\left(\alpha\left(\frac{b-a}{2}\right)\right) & \frac{\alpha}{\sqrt{1+\chi}}\cos\left(\frac{\alpha}{\sqrt{1+\chi}}(L-b)\right) \end{pmatrix} = 0. \tag{4.6}$$

Given L, a, b, ρ_m, this equation can be numerically solved to obtain α. In general, more than one solution will exist, but the smallest α is chosen since it corresponds to the fundamental mode. Then, f for the fundamental mode can be easily calculated using the expression for α.

To test our model, we numerically computed α and f for different mass loads and compared the results to those obtained from COMSOL Multiphysics FEM simulations. We defined $R =$

$\frac{M_load}{M_{unloaded}}$ and studied how α and f vary with this. This allowed us to study the behavior between no load ($R = 0$) and a load significantly larger than the unloaded resonator mass ($R \gg 1$). For our calculation, we chose a string with length $L = 1$ mm, width $w = 5$ μm, thickness $h = 110$ nm, and in-plane tensile stress $\sigma_0 = 0.700$ GPa. The mass-loaded region was located symmetrically at the center of the string with $b - a = 10$ μm. Finally, the material properties were chosen to match stoichiometric SiN with density $\rho_m = 3100$ kg/m^3, Young's modulus $E = 250$ GPa, and Poisson's ratio $\nu = 0.23$. On COMSOL, the film pre-patterning stress was set to a uniform value $\sigma_p = 1$ GPa such that the re-distributed stress after the stationary step was $\sigma_0 = 0.700$ GPa. The geometry was partitioned into the loaded and unloaded regions. We changed the density of the loaded region to be $\rho_m + \rho_M$ and swept the value of ρ_M over a wide range to change the mass load. We then computed the mode shapes and frequencies from our FEM simulation which involved a stationary stress redistribution study followed by an eigenfrequency study. Fig 4.1(c) shows how α (blue), and f (black), which we obtained by both numerical solution of our mass-loaded string model (solid lines) and through FEM simulations (solid circles), vary as a function of R. As visible, there is strong agreement between the two, thereby verifying our model and analysis. Interestingly, we note that as R increases, f continually decreases, but α appears to plateau.

To understand the implications of this α plateauing behavior, we can now try to analytically study the behavior of α in the limit of a large mass load. When $\sqrt{1+\chi}$ is very large, $\sin\left(\frac{\alpha}{\sqrt{1+\chi}}x\right) \approx \frac{\alpha}{\sqrt{1+\chi}}x$, and $\cos\left(\frac{\alpha}{\sqrt{1+\chi}}x\right) \approx 1$ for all $0 \leq x \leq L$. Using these approximations to simplify the matrix in Eq(4.5), and additionally, performing relevant row and column operations, we obtain the determinant equation

$$\det\begin{pmatrix} \alpha a & -\sin\left(\alpha\left(\frac{a-b}{2}\right)\right) & -\cos\left(\alpha\left(\frac{a-b}{2}\right)\right) & 0 \\ 1 & -\cos\left(\alpha\left(\frac{a-b}{2}\right)\right) & \sin\left(\alpha\left(\frac{a-b}{2}\right)\right) & 0 \\ 0 & \sin\left(\alpha\left(\frac{b-a}{2}\right)\right) & \cos\left(\alpha\left(\frac{b-a}{2}\right)\right) & -\alpha\left(L-b\right) \\ 0 & \cos\left(\alpha\left(\frac{b-a}{2}\right)\right) & -\sin\left(\alpha\left(\frac{b-a}{2}\right)\right) & 1 \end{pmatrix} = 0. \tag{4.7}$$

Simplifying this gives,

$$\cos\left(\alpha\left(a-b\right)\right)\left[-\left(L-\left(b-a\right)\right)\alpha+\left(1-a\left(L-b\right)\alpha^2\right)\tan\left(\left(a-b\right)\alpha\right)\right]=0, \tag{4.8}$$

which has the following two solutions:

$$\cos\left(\alpha\left(a-b\right)\right)=0 \tag{4.9}$$

$$\tan\left(\left(a-b\right)\alpha\right)=\frac{\left(L-\left(b-a\right)\right)\alpha}{\left(1-a\left(L-b\right)\alpha^2\right)}. \tag{4.10}$$

Eq(4.9) corresponds to higher order modes, while Eq(4.10) is for the fundamental mode. In the limit where the mass loaded region is small, we know $\left(b-a\right)\alpha \ll 1$. Using this Eq(4.10) can be solved for α which we shall now denote by α_{lim} to indicate it is the value of α for a very large mass load. We obtain

$$\alpha_{lim}=\sqrt{\frac{L}{a\left(b-a\right)\left(L-b\right)}}. \tag{4.11}$$

Thus, α_{lim} is in general a non-zero constant that depends on the geometric details of the mass-loaded string. This is possible because, as the mass load increases, the mode frequency f continually decreases while ρ_M increases. However, β_{lim}, which is the value of β in the limit of a large mass load, goes to zero because ρ_m is a constant. Fig 4.1(c) shows how α calculated from the numerical solution of our mass-loaded string model (solid blue line) and through FEM simulations (solid blue circles) both asymptote to the expected α_{lim} value (blue dotted line) which is given by Eq(4.11). In this high mass load regime, the pre-stressed Euler-Bernoulli beam equation simplifies to

$$\frac{l^2}{(2\pi)^2}\frac{d^4u}{dx^4}-\frac{d^2u}{dx^2}-K^2\left(x\right)u=0, \tag{4.12}$$

where now,

$$K^2(x)\approx\begin{cases}0 & \text{for } 0\leq x<a, \quad b<x\leq L\\ \alpha_{lim}^2 & \text{for } a\leq x\leq b\end{cases}. \tag{4.13}$$

Since this equation is independent of the mass load, the solution must also be independent of the mass load. This means in the limit of a large mass load, the mode shape must saturate to a constant shape. Fig 4.1(b) shows the mass-loaded string's fundamental mode shape normalized to its maximum displacement for different mass loads (lighter color indicates smaller mass load) as a function of the spatial coordinate along the string normalized to its length. The inset shows a magnified image of the mode shapes at the loaded region (shaded green). As visible, for a small mass load, the mode is approximately sinusodial, and as the mass increases the mode saturates to an approximately triangular shape as expected. The mode shapes for Fig 4.1(b) were obtained through COMSOL simulations. It worth mentioning that it is possible to analytically solve for the mode shape of a mass-loaded string [43, 42]. Since $Q_{bending}$ is purely a function of the mode shape for high-stress thin-film SiN resonators (see subection 2.2.3), this implies that with the mode shape, $Q_{bending}$ must also saturate. Fig 4.1(d) shows how $Q_{bending}$ for the string normalized to Q_0 which is its value when there is no mass load, varies as a function of R. As expected, we see that $Q_{bending}$ saturates. The $Q_{bending}$ values for this figure were calculated using the mode shapes obtained through COMSOL simulations, and to focus on the effect of the mass load, clamping losses were neglected.

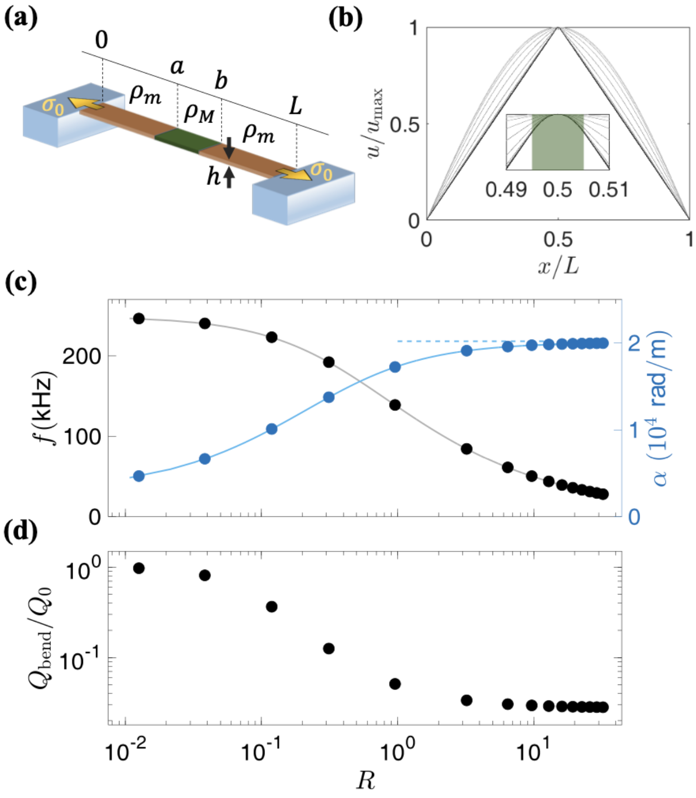

Figure 4.1: **Mass loaded string theoretical model.**

(a) String parameters: A string of length L, thickness h, with tensile stress σ_0 is fixed at the edges $x = 0$ and $x = L$, and has linear density ρ_m everywhere except for the region $a \leq x \leq b$, where the density is $\rho_M + \rho_m$. **(b)** Mode shape visualization: FEA simulations of the mass-loaded string fundamental mode normalized to its maximum displacement (lighter color corresponds to lighter mass load). Inset: mode shape at the loaded region (shaded green). **(c)** String frequency and inner region wavenumber: FEA simulated (solid circles) and analytically calculated (solid lines) fundamental mode frequency (black) and inner region wavenumber (blue) are shown as a function of R, the ratio between load mass total mass of the unloaded resonator, scanned by varying ρ_M while keeping a and b constant. Simulation points correspond to the mode shapes in **(b)**. Dashed blue line is the analytically calculated large mass limit inner region wavenumber α_{lim}. **(d)** String quality factor: fundamental mode $Q_{bending}$ normalized to Q_0, the $Q_{bending}$ of an unloaded resonator, as a function of R. To focus on mass loading effects, $Q_{bending}$ is calculated neglecting edge clamping loss. **(c)** and **(d)** share the horizontal coordinate, and results shown correspond to specific choice of parameters [42]. This figure is adapted from [43, 42].

4.1 Generalizing $Q_{bending}$ Saturation

While we have analytically demonstrated why mode shape and $Q_{bending}$ saturation occurs for the mass-loaded string, there is a more intuitive picture which will help us generalize $Q_{bending}$ saturation. There are two equivalent ways in which we can understand things. The first explanation is spatial: in the limit of a large load mass, the mode wavelength in the unloaded region $v_{unloaded}/f$, is much longer than the resonator's length scale. As a result, the mode shape in the outer regions does not curve, and for a string, the resulting limit shape is linear. Since the inner region has to match with the outer regions at the boundaries, the overall mode approaches a limit shape that is approximately triangular. The second explanation is temporal: for an unloaded resonator, the fundamental mode period is $T_{unloaded} = \frac{2L}{unloaded}$, which is the time it takes an out-of-plane disturbance to make a roundtrip across the resonator length L, with speed of sound $v_{unloaded}$. As the load mass increases, the mode period increases to $T_{loaded} = \frac{2(L-(b-a)))}{v_{unloaded}} + \frac{2(b-a)}{v_{load}}$. In the limit of a large load mass, since v_{load} is very small, the overall mode period is much larger than time taken for a disturbance to propogate in the unloaded regions. Therefore, the mode shape in the unloaded regions approximate a quasi-static displacement, with the limit shape being a static displacement at any moment. This leads to mode shape saturation which in turn implies $Q_{bending}$ saturation. Although we have focused on the case of a mass loaded string, the key points of the temporal argument above apply to highly tensioned resonators of arbitrary geometry and imply $Q_{bending}$ saturation for a high enough mass load. While it is possible to obtain analytical solutions for simple resonator geometries such as mass loaded strings, or mass loaded circular membranes [43, 42], in general analytical solutions may not exist, and we must resort ot FEM simulations.

In conclusion, we have investigated the simple toy model of a mass-loaded string. We have studied the dependence of the inner region wavenumber α, the fundamental mode's frequency f, shape, and $Q_{bending}$ of the on the mass load. In particular, we have shown that in the limit of a large mass load, α saturates, thereby leading to mode shape and $Q_{bending}$ saturation. Finally, we have compared the results from our analysis to FEM simulations and obtained strong agreement between the two. Although our analysis was specific the fundamental mode, the same approach can be applied to other modes. Further, we have provided an intuitive explanation of why mode shape and $Q_{bending}$ saturation occur, and we have generalized it to highly tensioned resonators of arbitrary geometry. In the next chapter, we will discuss an experiment we conducted to try and demonstrate $Q_{bending}$ saturation.

Chapter 5

Experimental Demonstration of $Q_{bending}$ Saturation

In order to validate the model predicted $Q_{bending}$ saturation effect, we designed a table-top experiment to study the effect of mass loading on the $Q_{bending}$ of a tensioned SiN mechanical resonator.

5.1 Experimental Plan

5.1.1 Resonator Choice - Trampoline

There exists a zoo of tensioned SiN mechanical resonator designs such as strings [14, 3], membranes [57, 54, 41], trampolines [26, 34], Silicon PnCs with a SiN membrane [52], and SiN PnCs with a defect [46, 32]. In general, any of these devices could be employed for a mass-loading experiment. Since the goal is to investigate the effect of mass loading on the $Q_{bending}$ of a resonator's modes, the obvious choice of a resonator is a PnC because the bandgap-confined modes of these devices are internal bending loss limited ($Q \approx Q_{bending}$). However, for practical chip-scale devices (not very large), the size of the bandgap is relatively small, and this means the mass loading studies must remain restricted to relatively small masses. In other words, the mode frequency decrease associated with using a large mass load will cause the modes to fall out of the bandgap where they are no longer protected from radiation loss. Since the goal is to understand how $Q_{bending}$ varies as we tune the mass load from a small value to something large (relative to the effective mode mass of the device), PnCs are an unsuitable platform to study the effect of mass loading on the $Q_{bending}$ of a tensioned mechanical resonator. Membranes are very sensitive to radiation loss [57] and we found through COMSOL FEM simulations that, as compared to devices like strings and trampolines, the reduction in $Q_{bending}$ is very large when membranes are mass loaded. In the case of strings, although they would be the appropriate device for our experiment, especially since our theoretical model is for that of a string, they are challenging to detect optically [14]. For these reasons, ultimately, we chose to use a trampoline resonator [26, 34] for our experiment. Trampolines are less prone to radiation loss than membranes, have a large pad for convenient optical detection, and are partially soft-clamped due to the fileted corners which results in high Q mechanical modes. Moreover, our initial COMSOL FEM simulations indicated that trampoline modes could have a large $Q_{bending}$ even when the mass load was large [43].

Our microfabricated fabricated trampoline resonators had a side length of 1 mm, a tether width of 5 μm, and a pad area of approximately 86 μm^2 (Fig 5.1). An unloaded fundamental mode frequency of $\approx$ 143 kHz was measured and agreed with COMSOL FEM simulations.

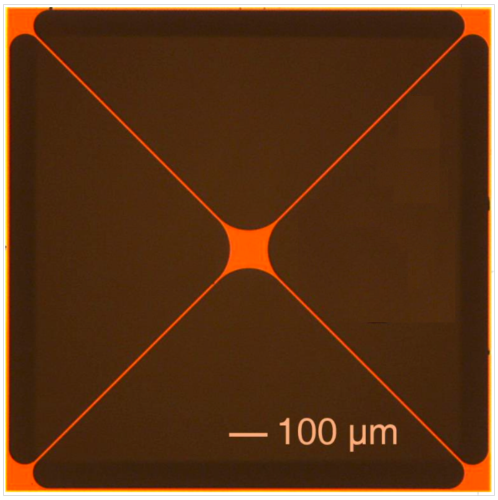

Figure 5.1: **Microscope image of device: SiN trampoline resonator. This figure is adapted from [43, 42].**

The orange regions represent SiN while the dark brown regions are empty space. The pad, tethers, filets, and frame of the trampoline device are seen. The silicon chip on which the device is suspended is not pictured.

The trampolines were microfabricated in the JILA cleanroom. A 375 μm thick, 3 inch diameter silicon wafer with 110 nm of stoichiometric LPCVD SiN on both sides was used. The SiN film was grown with a tensile stress of approximately 1 GPa. Direct write photolithography was used to pattern the resonator geometry and backside windows. A CF_4 reactive ion etch was used to complete patterning the SiN. O_2 plasma along with ultrasound sonication in an acetone bath were then used to clean the wafer. Finally, isopropyl alcohol and water were used for further cleaning. To release the SiN, the window side of the wafer was etched using a 80 C KOH bath.After the KOH weth etch, the wafer was cleaned using Nanostrip, followed by a solvent clean. Lastly, the devices were air dried.

5.1.2 Mass Loading - Magnetic Stacking

In order to study the effect of mass loading on the fundamental mode $Q_{bending}$ of a SiN trampoline resonator, we had to come up with a systematic method of mass loading a trampoline. Further, we had to be able to vary the mass over a wide range starting with a value much less than the effective mode mass, and going to a mass much larger than the same. We decided to use epoxy to affix a load mass to our device. Since epoxy is a very mechanically lossy substance, and different amounts of epoxy could lead to different amounts of loss, we decided to use a single trampoline device for the experiment with a single application of epoxy. For our mass load, we used magnetic grains. This was done because, once the first magnet is epoxied to the device, it can be magnetized, and additional magnets can be made to stick to the first, thereby providing an effective way to tune the mass load without the use of any additional epoxy. We called this technique *Magnetic Stacking.* Using a single trampoline device is also a good option since the Q of a trampoline can be significantly affected by dust particles, and the substrate silicon chip shape and size (due to coupling to substrate modes), both of which can vary from device to device. We worked in the JILA cleanroom to deposit magnets onto our trampoline resonator. We did this under a microscope using a 50x objective lens. Using tapered glass micropipettes (Product ID: Origio MAH-SM-0) attached to a micromanipulator, we applied ultra-violet (UV) epoxy (Product

ID: NEA 123SHGA) and deposited NeFeB magnets (Product ID: Neo Magnequech MQFP-B+ (D50=25m)) onto our devices. We used a UV flashlight to cure the epoxy. In order to perform magnetic stacking, we magnetized the grain(s) on our trampoline using a strong electromagnet ($B > 1\ T$). Although this field does not magnetically-saturate the grain(s), it is strong enough so as to allow us to perform magnetic stacking successfully. Between each addition of mass, the Q was measured. Fig 5.2 shows a trampoline device with a single magnetic grain, and Fig 5.3 shows a magnetic stack containing 4 magnets.

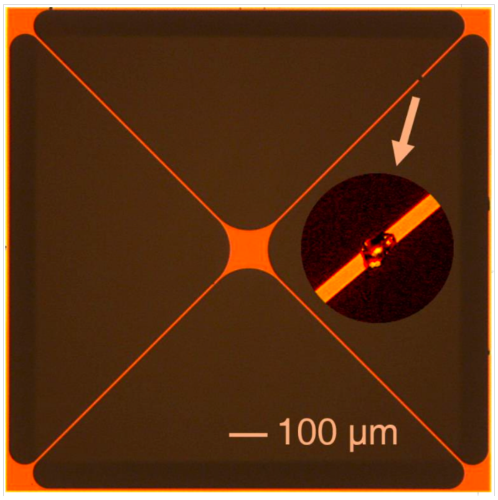

Figure 5.2: **SiN trampoline device with a magnetic grain.**

The images shows a trampoline resonator with a single magnetic grain. The inset shows a close up of the trampoline tether with the magnetic grain. This figure is adapted from [43, 42].

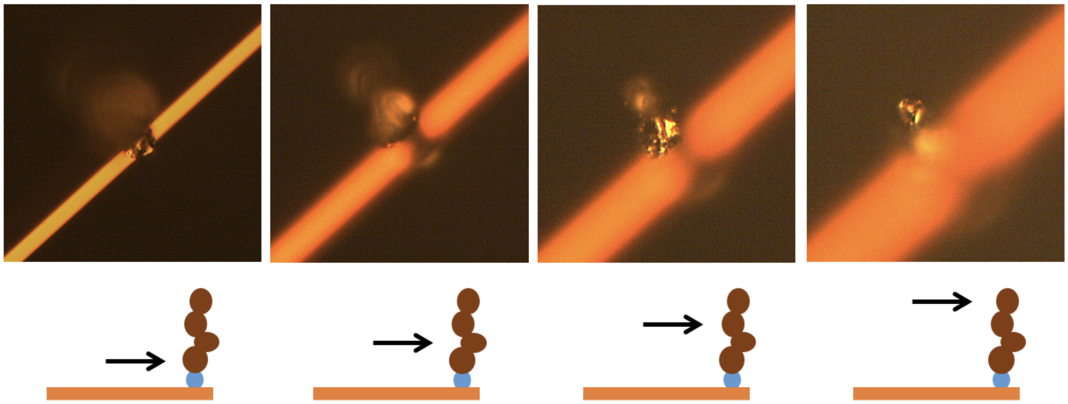

Figure 5.3: **SiN trampoline device with a magnetic stack.**

The images shows a trampoline resonator with magnetic stack containing 4 magnetic grains. Each image is taken in a different plane and depicts a different magnet. The cartoon indicates which magnetic in the stack is being seen. This figure is adapted from [43, 42].

5.1.3 Controlling Radiation Loss - Fixed Mounting

Although trampoline resonators are less susceptible to radiation loss than membranes [34, 26], they are still affected by it. Based on previously done experiments by research groups across the world, the method by which trampolines are mounted can significantly affect the fundamental mode Q [50, 27, 33]. In particular, the fundamental mode Q can decrease by orders of magnitude from its internal loss limited value when the device is rigidly held on a surface using any form of epoxy. As discussed previously, the highest Q values are obtained when the chip is placed under its own weight (see Sec. (2.3.3)). We tried a variety of different mounting experiments to find a suitable setup for the mass loading experiment. First, we tried using a silicon cross (Fig 5.4(a)) and mounted a silicon chip with a SiN trampoline (Fig 5.4(b)) on it either under its own weight (5.4(f))), or using a variable number of pieces of Kapton tape placed at different locations (Figs 5.4(c),(d),(e)).

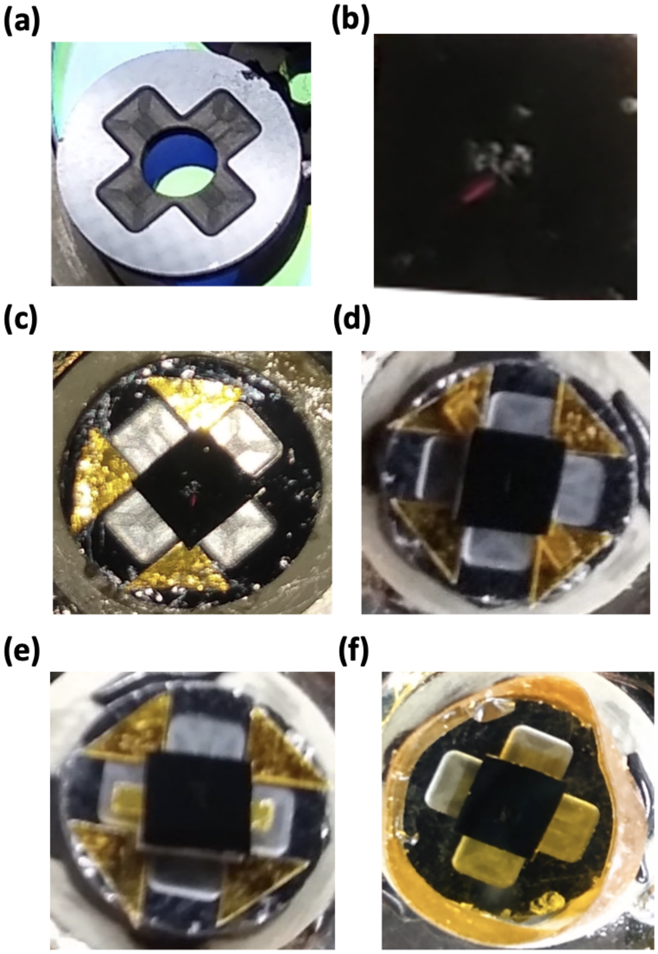

Figure 5.4: **SiN trampoline device mounting schemes on silicon cross.**
(a) Silicon cross for mounting. **(b)** Silicon chip with SiN trampoline at the center. The trampoline is not clearly visible. **(c)** Mounting of trampoline with Kapton tape at 3 corners. **(d)** Mounting of trampoline with Kapton tape at 2 opposite corners. **(e)** Mounting of trampoline with Kapton tape at 2 opposite sides. **(f)** Mounting of trampoline under its own weight.

The number of Kapton pieces were varied in order to understand if there was any obvious connection between radiation loss and the number of contact points where the chip was secured. Further, the location of the Kapton pieces were varied in order to check if securing the chip at mechanical nodes of hybridized trampoline-chip modes helped mitigate radiation loss. We also tried mounting a trampoline on a curved mirror to minimize the contact area (5.5(a))). Further, we tried mounting a trampoline on a low frequency beryllium copper spring which we hoped would act as a mechanical filter and reduce coupling between the trampoline mode and the environment (5.5(b))). Finally, we also tried epoxying a trampoline to a silicon chip mount at 1 corner using a small amount of silver epoxy (5.5(c))).

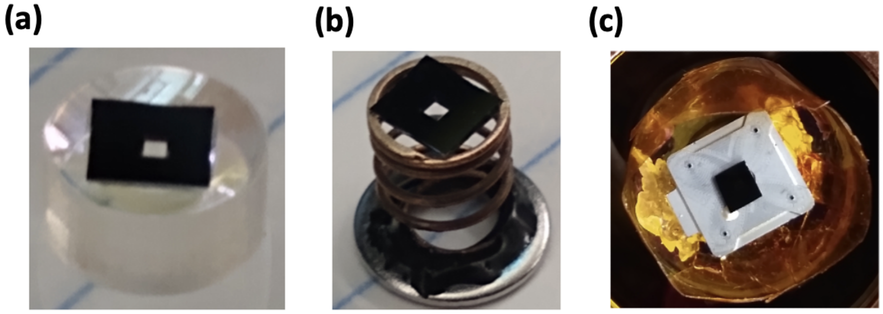

Figure 5.5: **Alternative SiN trampoline mounting schemes.**
(a) Mounting of trampoline on a curved mirror. **(b)** Mounting of trampoline on a low frequency beryllium copper spring. **(c)** Mounting of trampoline on a silicon frame with silver epoxy at 1 corner.

For each mounting scheme, we measured the fundamental mode Q of a trampoline resonator multiple times. The results are summarized in Fig 5.6. In each case, the highest measured Q is quoted since it corresponds to the lowest radiation loss. Further, the consistency of each mounting scheme is given and this indicates how repeatable the measurement is. Assuming reasonable parameters, the expected internal loss limited Q for our device was $Q = 30 \cdot 10^6$. Note that different mounting experiments used different trampoline devices, and it is therefore hard to draw strong conclusions because the presence of dirt and variable silicon chip shapes can significantly affect the fundamental mode Q.

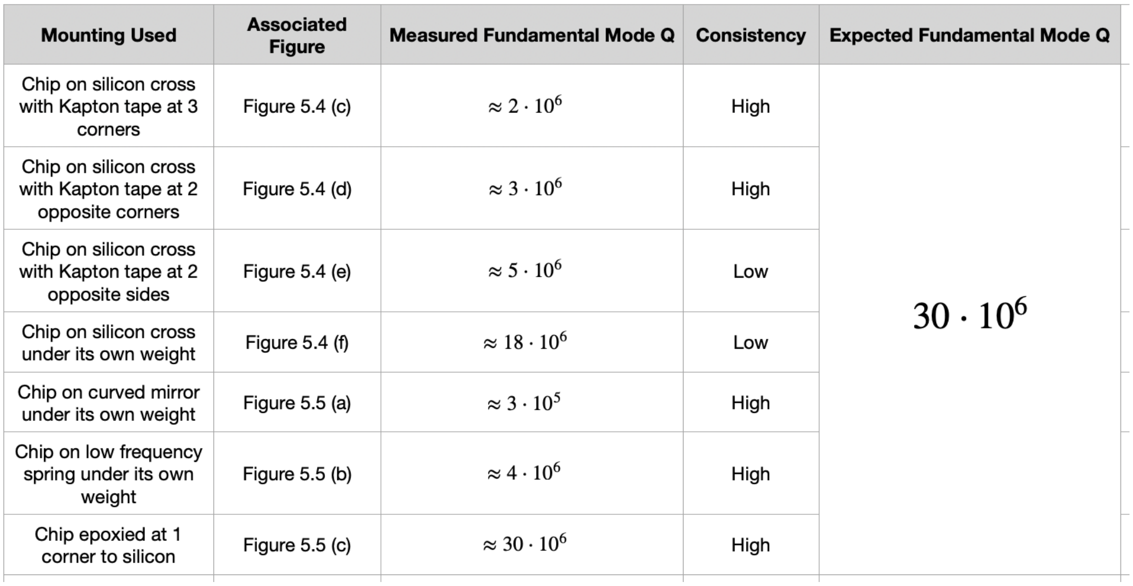

Mounting Used	Associated Figure	Measured Fundamental Mode Q	Consistency	Expected Fundamental Mode Q
Chip on silicon cross with Kapton tape at 3 corners	Figure 5.4 (c)	$\approx 2 \cdot 10^6$	High	$30 \cdot 10^6$
Chip on silicon cross with Kapton tape at 2 opposite corners	Figure 5.4 (d)	$\approx 3 \cdot 10^6$	High	
Chip on silicon cross with Kapton tape at 2 opposite sides	Figure 5.4 (e)	$\approx 5 \cdot 10^6$	Low	
Chip on silicon cross under its own weight	Figure 5.4 (f)	$\approx 18 \cdot 10^6$	Low	
Chip on curved mirror under its own weight	Figure 5.5 (a)	$\approx 3 \cdot 10^5$	High	
Chip on low frequency spring under its own weight	Figure 5.5 (b)	$\approx 4 \cdot 10^6$	High	
Chip epoxied at 1 corner to silicon	Figure 5.5 (c)	$\approx 30 \cdot 10^6$	High	

Figure 5.6: **Trampoline fundamental mode Q for different mounting schemes.** **(a)** Mounting of trampoline on a curved mirror. **(b)** Mounting of trampoline on a low frequency beryllium copper spring. **(c)** Mounting of trampoline on a silicon frame with silver epoxy at 1 corner.

In general we notice that reducing the number of contact points seems to increase the Q. However, the curved mirror result deviates from this trend. The low frequency spring does not appear to help in any way. When the chip is placed under its own weight on the silicon cross, the Q is quite high, and close to the expected Q. However, we found that in this setting, small changes in the position of the chip due to external vibrations (tapping on the vacuum chamber for example) could cause the Q to drop by an order of magnitude. Thus, placing the chip under its own weight turned out to be unsuitable for our experiment. This is because we need to be able to place the device in the same exact manner after a mass-loading sequence in the cleanroom, and this is impossible. We found that epoxying the chip to a silicon frame at 1 corner using silver epoxy gave a high Q close to the internal loss limited value. Moreover, we found that this mounting scheme was consistent in that multiple different trampolines mounted this way gave similar results. We named this mounting technique *Fixed Mounting* and decided to use it for the mass loading experiment.

5.2 Details of Implementation

5.2.1 Q Measurement

Fig. 5.7 shows the experimental setup which we used to measure the Q of our trampoline resonator. To read out the mechanical motion, we used an etalon interferometer with infra-red laser light of wavelength $\lambda = 1064$ nm. The etalon, which consists of two partially reflective surfaces, used the SiN as the first surface, and a Thorlabs beamsplitter as the second surface (BSS11 - Ø1" 30:70 (R:T) UVFS Plate Beamsplitter, Coating: 700 - 1100 nm, t = 5 mm). The reflection coefficient of the beamsplitter was chosen to match the reflection coefficient of SiN (roughly 30% for 100 nm), thereby maximizing the reflected optical power (this is a property of the etalon which can be mathematically proven). The distance between the SiN trampoline and the beamsplitter surface was roughly 3 cm. The mode frequencies were found by identifying peaks on the measured power spectrum. To find the mode Q values, we performed ringdown measurements by driving the resonator at the mode frequencies using a piezo-electric drive. The entire experiment was conducted inside a vacuum chamber. The chamber was pumped down initially using a roughing pump, followed by the use of an ion pump. The vacumm levels as read by the ion pump was $P < 10^{-7}$ Torr. Q measurements were conducted in this high-vacuum environment to prevent gas damping.

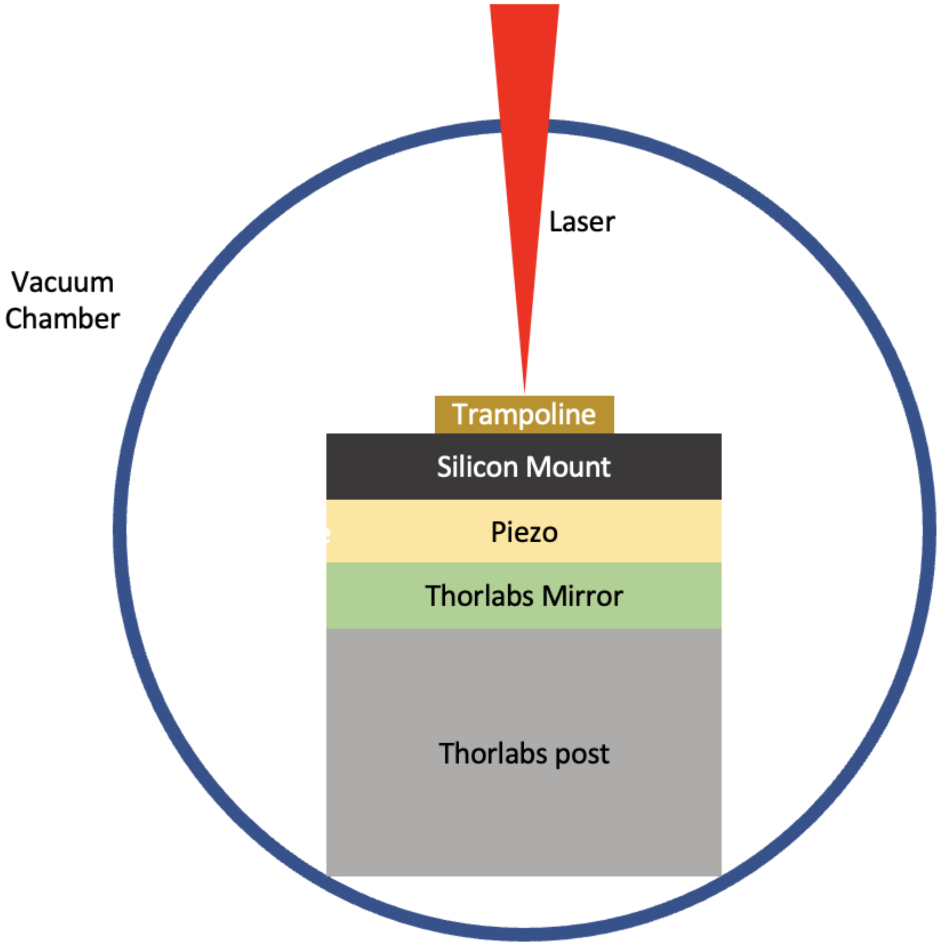

Figure 5.7: Q **Measurement Setup.**

A trampoline resonator is expoxied to a silicon mount and placed on a piezo. Under the piezo is a Thorlabs mirror/beamsplitter whcih has been glued to a Thorlabs post. The entire setup is in a vacuum chamber with optical access.

5.2.2 COMSOL Simulations

We used the Finite Element Method (FEM) Software COMSOL Multiphysics to calculate the trampoline mode frequencies and Q values. References [43, 42] contain all the required details on how to set up and carry out the simulations and process the relevant data. For additional guidance, the simulation files which were used in [43, 42] can be found at the following location: S:\regal\common\LabData\Optomechanics \Manuscripts\Mass_Loading_Paper\Final COMSOL simulations for mass-loading paper figures.

In this subsection, I will provide some important guidelines to obtain accurate results in terms of meshing and plugging in relevant parameters on COMSOL. Without a doubt, meshing is the most important factor. Assuming the simulation is set up correctly, inadequate meshing is the most common reason for simulation results that do not converge and/or disagree with theory. We can refer back to Equations (3.6) to gain some insight. The key is to notice that the loss depends sensitively on the integrated mean curvature over the mode shape. Thus, the more the curvature, the more the loss, and the lower the $Q_{bending}$. Therefore, we must accurately capture the curvature in regions where it is high.

For “hard-clamped” resonators such as membranes, strings, and trampolines, there is a very sharp kink in the mode shape near the clamped boundary edge (due to a fourth-order term which arises from Euler-Bernoulli beam theory and Kirchhoff–Love plate theory, see Fig. 3.1). If the edges are not meshed very carefully, it becomes impossible to reproduce $Q_{bending}$ values that make sense. The standard approach is to carefully partition the COMSOL CAD geometry into regions where the curvature is expected to be low and high and then mesh each separately. The low-curvature regions can be meshed coarsely, and the high-curvature regions need to be meshed finely. A foolproof method to check the reliability of the $Q_{bending}$ numbers is to perform a mesh convergence study - repeatedly refine the mesh over ALL parts of the resonator geometry until $Q_{bending}$ stops varying by a significant amount. Figs. 5.8 and 5.9 below show how to efficiently partition and mesh a trampoline resonator. Notice that the partitioning is done to isolate the low and high curvature regions. The meshing at the edge gets progressively finer in order to accurately capture the bending. Note that the length scale of the high curvature region can be calculated analytically [14] and it is typically around 3 μm for a 500 μm membrane device but varies from device to device.

Similar partitioning and meshing strategies can be used for strings, membranes, and other devices. For mass-loaded devices, the meshing needs to be fine inside the epoxy and the regions of the resonator surrounding the epoxy, but not necessarily inside the mass load itself. Once again, a mesh convergence needs to be performed to ensure reliability.

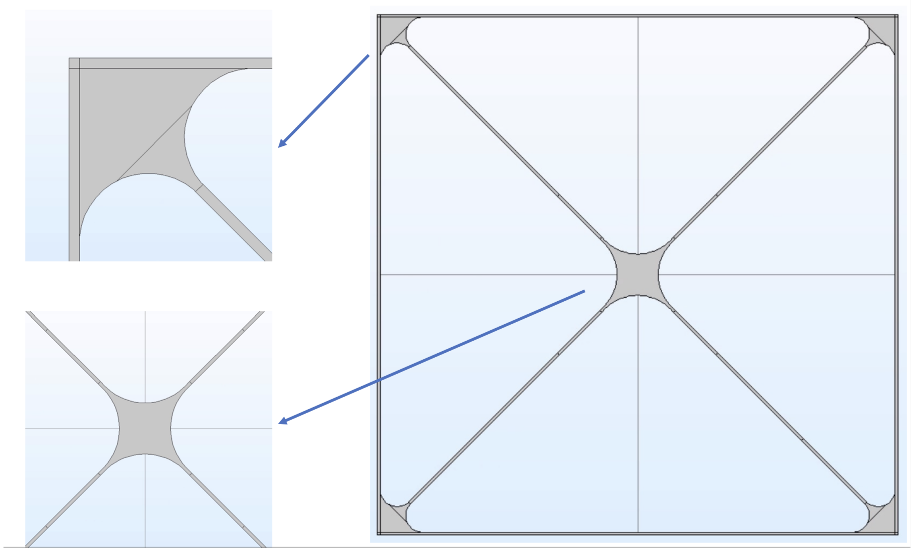

Figure 5.8: **Trampoline Geometry Partitioning on COMSOL.**

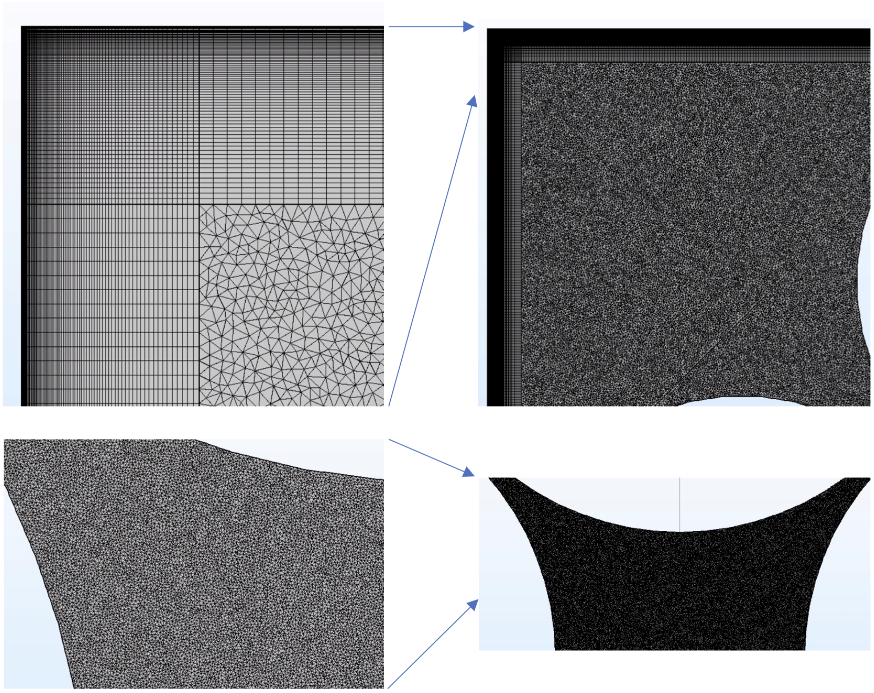

Figure 5.9: **Trampoline Geometry Meshing on COMSOL.**

As a final note to the future COMSOLer who may find this useful, a lot of old COMSOL simulation files use a volume integral of the kinetic energy density "Solid.Wk" to find the energy W of the mode. However, this is incorrect as it gives the average energy (over one motional cycle I think), so you should actually use 2 times this result for W!

5.3 Experimental Results and Additional Simulations

The results of our experiment along with relevant FEM simulations are shown in Fig 5.10. We see Q_{fund} and f, which are the trampoline resonator fundamental mode Q and frequency respectively, as a function of the load mass.

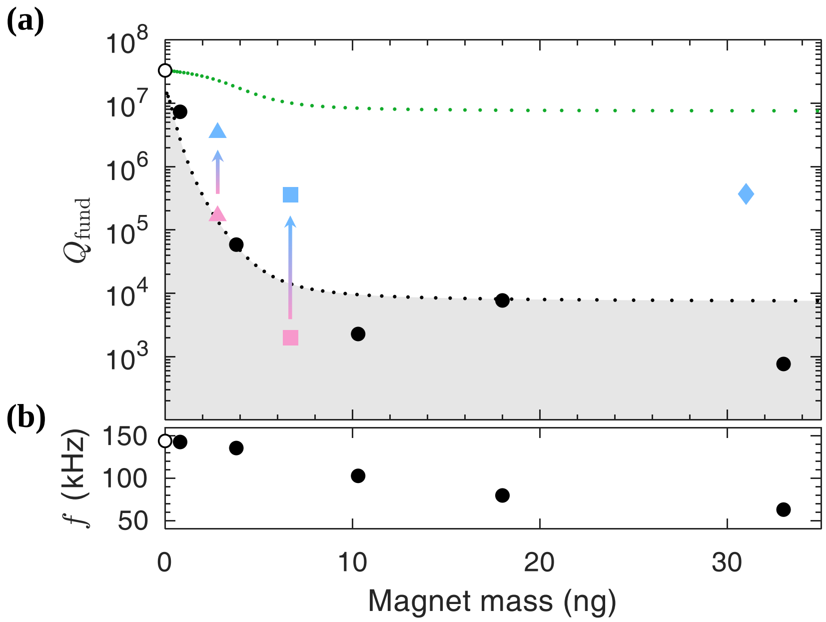

Figure 5.10: **Experimental results and FEM simulations.**

(a) Q_{fund} as a function of magnet mass: Measured Q_{fund} at 300 K (circles) unloaded (open black circle) and with a varying load (solid black circles). Corresponding FEA simulated $Q_{bending}$ results disregarding (green dotted line) and including (black dotted line) epoxy loss. The shaded area accounts for other possible losses, e.g. radiation loss. Measured Q_{fund} for additional two devices (triangle and square) are shown at both 300 K (light pink) and 8 K (sky blue). Measured Q_{fund} for a third device with a large load mass at 8 K is also shown (sky blue diamond). **(b)** Fundamental mode frequency as a function of magnet mass: Frequency measurements at 300 K (circles) corresponding to data points in (a). This figure is adapted from [43, 42].

We performed the magnetic stacking experiment described in the previous chapter and used that to measure the trampoline's Q_{fund} and frequency as a function of the mass.

Fig. 5.10(b) shows how the resonator frequency varies with the added mass at 300 K (circles). The frequencies were found by looking for peaks on the motional noise power spectral density. The added mass was back-calulated by using the frequency shifts from the unloaded resonator frequency (open black circle) This allowed us to calibrate the rest of the measurements.

Fig. 5.10(a) shows how the resonator Q_{fund} varies with the added mass. Open black circle and solid black circles relate to the Q_{fund} values for a trampoline at 300 K, without and with a variable mass load. Q_{fund} decreases as the mass increases, but plateaus for masses larger than $\sim 10\,\text{ng}$ (which is much larger than the effective mass ($\sim 4\,\text{ng}$) of the unloaded resonator). This indicates the theory predicted $Q_{bending}$ saturation effect. This saturated Q_{fund} value is approximately four orders of magnitude lower than the unloaded Q_{fund}.

We used FEM simulations to model these results. We accounted for bending loss in both the SiN and the epoxy, while disregarding radiation loss (black dotted line). The epoxy length scale and loss tangent were scanned to choose realistic model parameters to obtain reasonable agreement between our simulation measured data, while also setting an upper bound on Q_{fund} [42]. Our simulation is used as an upper bound for the results as, irrespective of device mounting, at higher mass (lower frequency), the resonator is more susceptible to radiation loss.

To validate that the large reduction in Q_{fund} originates primarily from epoxy loss rather than spurious radiation loss, we performed additional measurements on two different devices (triangle and square) both at 300 K and 8 K (light pink and sky blue markers respectively). The measured Q_{fund} rises by two orders of magnitude for resonators cooled to 8 K. Although SiN resonators are expected to have reduced bending loss at 8 K compared to 300 K, it is by a factor of ~ 3, which cannot explain these observations [32]. We therefore conclude that when cold, the epoxy loss reduces significantly, affirming the reduction in Q_{fund} is primarily due to loss in the epoxy. This is true for small masses, however, the situation is a bit more complicated at large masses where we expect radiation loss to be more dominant. Thus, a fourth device (sky blue diamond) measured at 8 K provides evidence that a fairly high quality factor ($Q_{fund} \approx 3.7 \times 10^5$) can be achieved in the saturated regime. Once again, (although we are comparing different devices) this is orders of magnitude larger than the room temperature measurements at similar masses, thus confirming that even at large masses, epoxy loss is the dominant form of loss and radiation loss can be mostly ignored. Moreover, this is in agreement with measurements from [23], presented as blue stars in Fig. 5.10.

In order to set a theoretical limit on the saturated Q_{fund} at 300 K, we performed FEM simulations that include only SiN bending loss and disregard all other forms of loss (green dotted line). The results show $Q_{bending}$ as high as 10^7 is possible in the limit of a large load mass. The saturated $Q_{bending}$ for trampolines can be improved with mass load location optimization [42] and possibly by using trampoline resonators with carefully engineered geometries [26, 34, 17].

In Fig. 5.11, we see how varying the position of the mass load on the trampoline affects the saturated Q_{fund} value. We find that the $Q_{bending}$ saturates to a higher value when the mass load is on a tether rather than the trampoline pad. Further, we find the optimal location for mass loading to be the tether region near the trampoline pad. As a clarification, when calculating these results, we disregarded loss inside the epoxy and only considered loss in the SiN. This can be used to optimize the functionalized resonator for sensing applications.

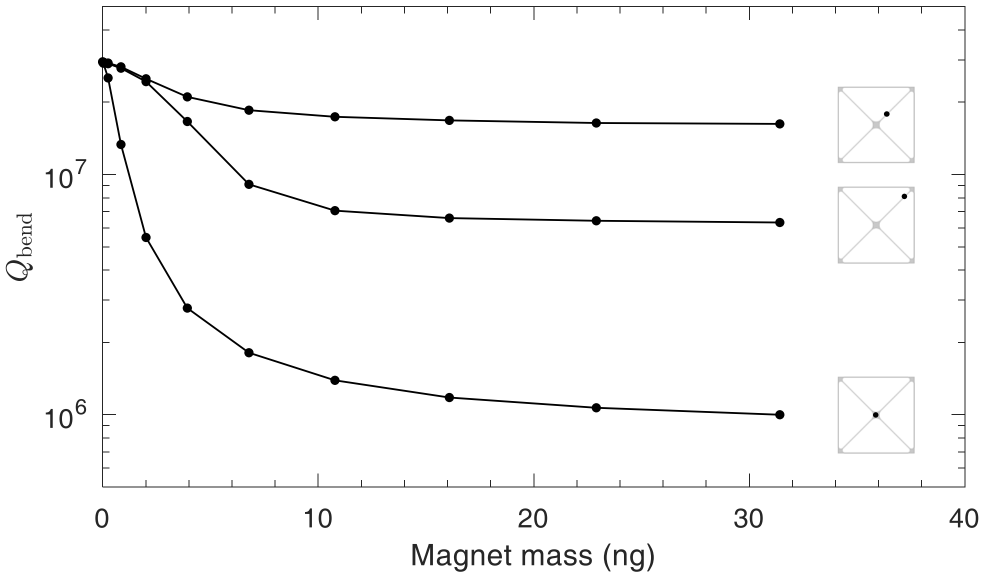

Figure 5.11: **Trampoline $Q_{bending}$ as a function of magnet mass and location.** The plots show $Q_{bending}$ for trampolines as a function of the magnet mass and location (solid black circles with black lines). The insets (small trampolines marked with a black circle) indicate the location of the mass load in each case. For each of the three curves, the solid black circles represent FEA simulation data, and we have drawn a line joining them to indicate the general trend with increasing mass load. This figure is adapted from [43, 42].

It is also interesting to study the effect of varying the nitride thickness. For soft clamped resonators $Q_{bending} \propto h^{-1}$ [46, 32] and because trampolines can be considered as partially soft-clamped resonators, we expect that $Q_{bending}$ reduces with increasing thickness. However, when a mass load is present we find the situation is more complicated. For small masses, the mode shape barely changes, and in this situation, as expected, thinner SiN offers the best $Q_{bending}$ values. But as the mass increases, we observe a transition in the trend, and surprisingly, for intermediate masses, thicker SiN leads to the highest $Q_{bending}$ values. However, in the limit of a large mass load, thinner SiN leads to the highest $Q_{bending}$ values. But in this regime, it appears that $Q_{bending}$ saturates to approximately the same value irrespective of the SiN thickness. Once again, when calculating these results, to clarify, we disregarded loss inside the epoxy and only included bending loss in the SiN.

The results are illustrated in Fig. 5.12

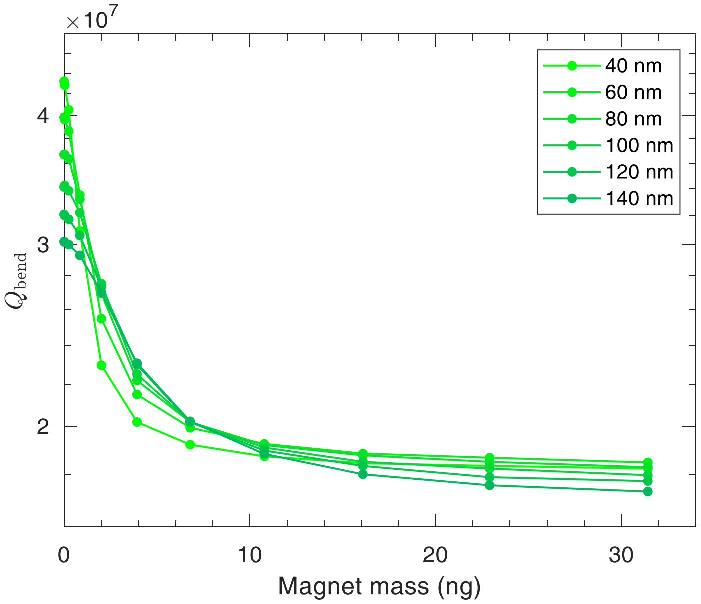

Figure 5.12: $Q_{bending}$ **as a function of magnet mass for different SiN thicknesses.** The plots show $Q_{bending}$ as a function of magnet mass for different SiN thicknesses (colored green circles with colored green lines). The legend (top right) indicates the nitride thickness (the lightest shade of green corresponds to the thinnest SiN while the darkest corresponds to the thickest). For each of the curves, the solid points represent simulation data, and we have drawn a line joining them to indicate the general trend with increasing mass load. This figure is adapted from [43, 42].

Besides trampolines, there is interest to study the effect of mass-loading on soft clamped devices such as defect containing phononic crystals. There are advantages because these devices are radiation loss protected ($Q \approx Q_{bending}$) due to the presence of an acoustic bandgap, and further, they are soft clamped. Thus they do not need to be mounted in any special manner [32, 46], and they have ultrahigh Q modes to begin with. Although studies must be limited to relatively small masses, this is relevant in certain applications such as microscopy [16] where there is no need to put a large mass on the resonator (for instance one could put the sample on the resonator rather than the magnet). We performed COMSOL simulations to find the effect of mass-loading on the Q of the defect mode of the "flower" style defect phononic crystal [32]. We varied the location of the mass load to learn how to optimize the Q, but we did not change the size of the mass since this could easily cause the defect mode to fall out of the bandgap. We used a fixed mass of 0.25 ng which is the largest mass one can use without making the defect mode to fall out of the bandgap. The overall device size was such that the fundamental defect mode frequency was 0.5 MHz. Fig. 5.13 shows a SIN phononic crystal with a "flower" style defect [32]. Fig. 5.14 shows the shape of fundamental defect mode when there is no mass load (no kinks).

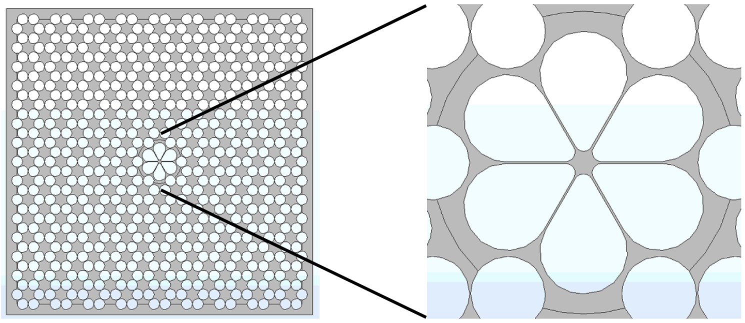

Figure 5.13: **SiN Phononic Crystal with a "Flower" Style Defect.**

The image shows the SiN phononic crystal (left) with a "flower" style defect (right).

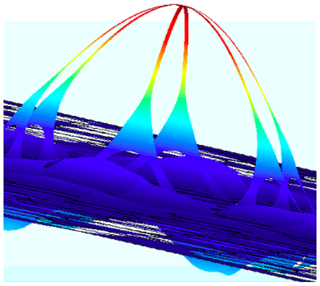

Figure 5.14: **Mass-Free Fundamental Defect Mode of a SiN Phononic Crystal with a "Flower" Style Defect.**

The image shows the fundamental mode of a SiN phononic crystal with a "flower" style defect when there is no mass load.

When a mass-load is added to the center of the "flower" pad, Fig. 5.15 shows how the mode shape changes. As visible, there is now a sharp kink in the mode shape near the pad, and based on Equation 3.6, we know the Q must drop.

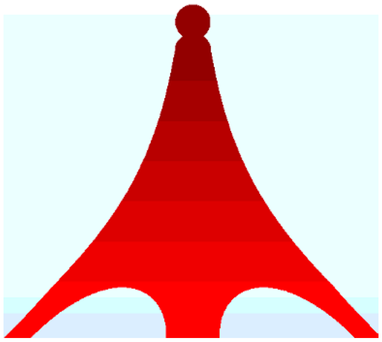

Figure 5.15: **Mass-Loaded Fundamental Defect Mode of a SiN Phononic Crystal with a "Flower" Style Defect.**

The image shows the fundamental mode of a SiN phononic crystal with a "flower" style defect when there is a mass load at the pad center.

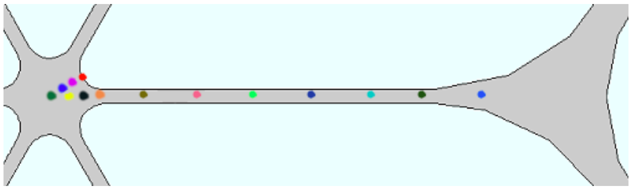

Figure 5.16: **Locations of Mass Loading on Defect.**

The image shows the locations on the defect (colored dots) at which the effect of mass-loading was studied.

Next, as depicted in Fig. 5.17, we placed a fixed size mass of 0.25 ng at different locations on the defect of the phononic crystal and computed the Q (Fig. **??**).

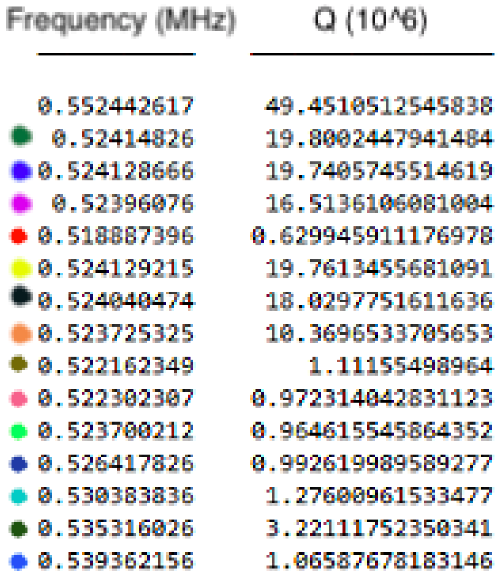

	Frequency (MHz)	Q (10^6)
	0.552442617	49.4510512545838
●	0.52414826	19.8002447941484
●	0.524128666	19.7405745514619
●	0.52396076	16.5136106081004
●	0.518887396	0.629945911176978
●	0.524129215	19.7613455681091
●	0.524040474	18.0297751611636
●	0.523725325	10.3696533705653
●	0.522162349	1.11155498964
●	0.522302307	0.972314042831123
●	0.523700212	0.964615545864352
●	0.526417826	0.992619989589277
●	0.530383836	1.27600961533477
●	0.535316026	3.22111752350341
●	0.539362156	1.06587678183146

Figure 5.17: Q **as a Function of Mass Loading on Defect.**

The image shows how the location of mass loading (colored dots corresponding to specific locations shown on Fig. 5.17) on the phononic crystal defect affects the Q of the fundamental mode. The topmost row corresponds to the situation without a mass load.

In general, as expected, no matter where the mass load is placed the Q seems to drop. However, we notice the Q decreases by a lot when the defect tether has a mass load on it and less so when the pad has a mass load on it. This is rather unintuitive because the trend appears to be the opposite in the trampoline. In general the effect of mass loading is complicated since a mass-load significantly distorts the mode shape, and the Q is inversely related to the overall integrated curvature. However, it should also be noted that this set of results may have something to do with the fact that the phononic crystal is strongly soft-clamped while the trampoline is only slightly soft-clamped. A further study would be required to draw meaningful conclusions.

5.4 Implications of $Q_{bending}$ Saturation

As seen, we have shown through analytic, computational and experimental methods that in the limit of a large mass load, $Q_{bending}$ saturates. Looking back at Equation (2.15), we see this implies something very interesting:

$$S_\beta = \sqrt{\frac{4k_bTk^{\frac{1}{2}}}{M^{\frac{3}{2}}Q}} = \psi M^{-\frac{3}{4}}. \tag{5.1}$$

Here, ψ is just a constant. Thus, S_β, which is the thermal limited sensitivity for measuring β scales as $M^{-\frac{3}{4}}$. This means that using a larger mass can enhance sensitivity by lowering the thermal noise! This is particularly relevant for applications such as chip scale accelerometry, and fundamental physics experiments such as quantum gravity measurements [56, 23].

Chapter 6

Conclusion

In this work, we study the effect of a localized mass load on the $Q_{bending}$ of highly tensioned SiN resonators. We show through analytical calculations and finite element analysis (FEM) that as the load mass increases, the modes of the resonator change in frequency and shape. Further, we show that for a large enough mass, each mode shape becomes independent of the mass, which leads to mass-independent $Q_{bending}$. We refer to this phenomenon as $Q_{bending}$ saturation. We validate this saturation experimentally by measuring the Q of a tensioned SiN trampoline resonator as a function of the load mass. By carefully controlling loss channels besides bending loss, we enable comparisons between Q measurements for different load masses on a single device. To vary the load mass, we use magnetic grains for the load mass, and we sequentially stack the grains using their mutual magnetic attraction. We use a low-finesse Fabry-Perot interferometer and perform ringdowns in a high vacuum environment to measure the Q of the resonators. We compare our experimental results to finite element method (FEM) simulations performed on COMSOL Multiphysics and see good agreement. Through our experiment, we successfully demonstrate $Q_{bending}$ saturation.

A direct result of $Q_{bending}$ saturation is the scaling $S_\beta \propto M^{-\frac{3}{4}}$, suggesting that at the large mass limit, the sensitivity S_β scales favorably with mass. This could enable improved sensing capabilities in resonators for magnetic force detection, accelerometer, and future-term gravitational sensors.

Future work could involve more in-depth studies on how to obtain ultrahigh Q resonators with a large mass load. This could be approached by developing new fabrication methods which allow for mass deposition without the use of a lossy intermediate like epoxy, and combining it with newly emerging design methods such as inverse design [17] or physics-informed neural networks [31].

Bibliography

[1] Reed W Andrews, Robert W Peterson, Tom P Purdy, Katarina Cicak, Raymond W Simmonds, Cindy A Regal, and Konrad W Lehnert. Bidirectional and efficient conversion between microwave and optical light. Nature Physics, 10(4):321–326, 2014.

[2] Markus Aspelmeyer, Tobias J Kippenberg, and Florian Marquardt. Cavity optomechanics. Reviews of Modern Physics, 86(4):1391, 2014.

[3] Mohammad J Bereyhi, Alberto Beccari, Sergey A Fedorov, Amir H Ghadimi, Ryan Schilling, Dalziel J Wilson, Nils J Engelsen, and Tobias J Kippenberg. Clamp-tapering increases the quality factor of stressed nanobeams. Nano Letters, 19(4):2329–2333, 2019.

[4] Mohammad J Bereyhi, Alberto Beccari, Robin Groth, Sergey A Fedorov, Amirali Arabmoheghi, Tobias J Kippenberg, and Nils J Engelsen. Hierarchical tensile structures with ultralow mechanical dissipation. Nature Communications, 13(1):1–9, 2022.

[5] A Borrielli, L Marconi, F Marin, F Marino, B Morana, G Pandraud, A Pontin, GA Prodi, PM Sarro, E Serra, et al. Control of recoil losses in nanomechanical sin membrane resonators. Physical Review B, 94(12):121403, 2016.

[6] Daniel WC Brooks, Thierry Botter, Sydney Schreppler, Thomas P Purdy, Nathan Brahms, and Dan M Stamper-Kurn. Non-classical light generated by quantum-noise-driven cavity optomechanics. Nature, 488(7412):476–480, 2012.

[7] CL Degen, M Poggio, HJ Mamin, CT Rettner, and D Rugar. Nanoscale magnetic resonance imaging. Proceedings of the National Academy of Sciences, 106(5):1313–1317, 2009.

[8] KL Ekinci, XMH Huang, and ML Roukes. Ultrasensitive nanoelectromechanical mass detection. Applied Physics Letters, 84(22):4469–4471, 2004.

[9] Sergey A Fedorov, Alberto Beccari, Nils J Engelsen, and Tobias J Kippenberg. Fractal-like mechanical resonators with a soft-clamped fundamental mode. Physical Review Letters, 124(2):025502, 2020.

[10] Sergey A Fedorov, Nils J Engelsen, Amir H Ghadimi, Mohammad J Bereyhi, Ryan Schilling, Dalziel J Wilson, and Tobias J Kippenberg. Generalized dissipation dilution in strained mechanical resonators. Physical Review B, 99(5):054107, 2019.

[11] Ran Fischer, Dylan P McNally, Chris Reetz, Gabriel GT Assumpcao, T Knief, Yiheng Lin, and Cindy A Regal. Spin detection with a micromechanical trampoline: towards magnetic resonance microscopy harnessing cavity optomechanics. New Journal of Physics, 21(4):043049, 2019.

[12] Moritz Forsch, Robert Stockill, Andreas Wallucks, Igor Marinković, Claus Gärtner, Richard A Norte, Frank van Otten, Andrea Fiore, Kartik Srinivasan, and Simon Gröblacher. Microwave-to-optics conversion using a mechanical oscillator in its quantum ground state. Nature Physics, 16(1):69–74, 2020.

[13] Amir H Ghadimi, Sergey A Fedorov, Nils J Engelsen, Mohammad J Bereyhi, Ryan Schilling, Dalziel J Wilson, and Tobias J Kippenberg. Elastic strain engineering for ultralow mechanical dissipation. Science, 360(6390):764–768, 2018.

[14] Amir Hossein Ghadimi, Dalziel Joseph Wilson, and Tobias J Kippenberg. Radiation and internal loss engineering of high-stress silicon nitride nanobeams. Nano Letters, 17(6):3501–3505, 2017.

[15] Gabriela I González and Peter R Saulson. Brownian motion of a mass suspended by an anelastic wire. The Journal of the Acoustical Society of America, 96(1):207–212, 1994.

[16] David Hälg, Thomas Gisler, Yeghishe Tsaturyan, Letizia Catalini, Urs Grob, Marc-Dominik Krass, Martin Héritier, Hinrich Mattiat, Ann-Katrin Thamm, Romana Schirhagl, et al. Membrane-based scanning force microscopy. Physical Review Applied, 15(2):L021001, 2021.

[17] Dennis Høj, Fengwen Wang, Wenjun Gao, Ulrich Busk Hoff, Ole Sigmund, and Ulrik Lund Andersen. Ultra-coherent nanomechanical resonators based on inverse design. Nature Communications, 12(1):1–8, 2021.

[18] Prashanta Kharel, Yiwen Chu, Michael Power, William H Renninger, Robert J Schoelkopf, and Peter T Rakich. Ultra-high-q phononic resonators on-chip at cryogenic temperatures. 3(6):066101, 2018.

[19] Alexander G Krause, Martin Winger, Tim D Blasius, Qiang Lin, and Oskar Painter. A high-resolution microchip optomechanical accelerometer. Nature Photonics, 6(11):768–772, 2012.

[20] Nickolay V Lavrik and Panos G Datskos. Femtogram mass detection using photothermally actuated nanomechanical resonators. Applied physics letters, 82(16):2697–2699, 2003.

[21] LANDAU LD and EM LIFSHITZ. Course of theoretical physics. theory of elasticity. 1975.

[22] Zongyang Li, Qiang Zhang, Xiang You, Yongmin Li, and Kunchi Peng. Suppression of phonon tunneling losses by microfiber strings for high-q membrane microresonators. Applied Physics Letters, 109(19):191903, 2016.

[23] Yulong Liu, Jay Mummery, Jingwei Zhou, and Mika A Sillanpää. Gravitational forces between nonclassical mechanical oscillators. Physical Review Applied, 15(3):034004, 2021.

[24] Gregory S MacCabe, Hengjiang Ren, Jie Luo, Justin D Cohen, Hengyun Zhou, Alp Sipahigil, Mohammad Mirhosseini, and Oskar Painter. Nano-acoustic resonator with ultralong phonon lifetime. Science, 370(6518):840–843, 2020.

[25] Mohammad Mirhosseini, Alp Sipahigil, Mahmoud Kalaee, and Oskar Painter. Superconducting qubit to optical photon transduction. Nature, 588(7839):599–603, 2020.

[26] Richard A Norte, Joao P Moura, and Simon Gröblacher. Mechanical resonators for quantum optomechanics experiments at room temperature. Physical Review Letters, 116(14):147202, 2016.

[27] Richard Alexander Norte. Nanofabrication for on-chip optical levitation, atom-trapping, and superconducting quantum circuits. PhD Thesis, 2015.

[28] J. R. Pratt, A. R. Agrawal, C. A. Condos, C. M. Pluchar, S. Schlamminger, and D. J. Wilson. Nanoscale torsional dissipation dilution for quantum experiments and precision measurement. Phys. Rev. X, 13:011018, Feb 2023.

[29] Jon R Pratt, Aman R Agrawal, Charles A Condos, Christian M Pluchar, Stephan Schlamminger, and Dalziel J Wilson. Nanoscale torsional dissipation dilution for quantum experiments and precision measurement. arXiv preprint arXiv:2112.08350, 2021.

[30] Thomas P Purdy, P-L Yu, Robert W Peterson, Nir S Kampel, and Cindy A Regal. Strong optomechanical squeezing of light. Physical Review X, 3(3):031012, 2013.

[31] Maziar Raissi, Paris Perdikaris, and George E Karniadakis. Physics-informed neural networks: A deep learning framework for solving forward and inverse problems involving nonlinear partial differential equations. Journal of Computational physics, 378:686–707, 2019.

[32] Chris Reetz, Ran Fischer, Gabriel GT Assumpcao, Dylan P McNally, Peter S Burns, Jack C Sankey, and Cindy A Regal. Analysis of membrane phononic crystals with wide band gaps and low-mass defects. Physical Review Applied, 12(4):044027, 2019.

[33] Christoph Reinhardt. Ultralow-noise silicon nitride trampoline resonators for sensing and optomechanics. PhD Thesis, 2017.

[34] Christoph Reinhardt, Tina Müller, Alexandre Bourassa, and Jack C Sankey. Ultralow-noise sin trampoline resonators for sensing and optomechanics. Physical Review X, 6(2):021001, 2016.

[35] Daniel Rugar, Raffi Budakian, HJ Mamin, and BW Chui. Single spin detection by magnetic resonance force microscopy. Nature, 430(6997):329–332, 2004.

[36] Amir H Safavi-Naeini, Simon Gröblacher, Jeff T Hill, Jasper Chan, Markus Aspelmeyer, and Oskar Painter. Squeezed light from a silicon micromechanical resonator. Nature, 500(7461):185–189, 2013.

[37] SW Schediwy, Slawomir Gras, Li Ju, and DG Blair. High q factor bonding using natural resin for reduced thermal noise of test masses. Review of scientific instruments, 76(2):026117, 2005.

[38] Silvan Schmid, Luis Guillermo Villanueva, and Michael Lee Roukes. Fundamentals of nanomechanical resonators, volume 49. Springer, Berlin, 2016.

[39] Jonas Schmöle, Mathias Dragosits, Hans Hepach, and Markus Aspelmeyer. A micromechanical proof-of-principle experiment for measuring the gravitational force of milligram masses. Classical and Quantum Gravity, 33(12):125031, 2016.

[40] Nicolas Scozzaro, William Ruchotzke, Amanda Belding, Jeremy Cardellino, Erick C Blomberg, Brendan A McCullian, Vidya P Bhallamudi, Denis V Pelekhov, and P Chris Hammel. Magnetic resonance force detection using a membrane resonator. Journal of Magnetic Resonance, 271:15–20, 2016.

[41] Enrico Serra, M Bawaj, A Borrielli, G Di Giuseppe, S Forte, N Kralj, N Malossi, L Marconi, F Marin, F Marino, et al. Microfabrication of large-area circular high-stress silicon nitride membranes for optomechanical applications. AIP Advances, 6(6):065004, 2016.

[42] R. Shaniv, S. Keshava, C. Reetz, and C.A. Regal. Supplemental material to understanding the quality factor of mass-loaded tensioned resonators. Physical Review Applied, 19, 03 2023.

[43] R. Shaniv, S. Keshava, C. Reetz, and C.A. Regal. Understanding the quality factor of mass-loaded tensioned resonators. Physical Review Applied, 19, 03 2023.

[44] Dongil Shin, Andrea Cupertino, Matthijs HJ de Jong, Peter G Steeneken, Miguel A Bessa, and Richard A Norte. Spiderweb nanomechanical resonators via bayesian optimization: inspired by nature and guided by machine learning. Advanced Materials, 34(3):2106248, 2022.

[45] John R Taylor. Classical mechanics. 3 “e ed.

[46] Yeghishe Tsaturyan, Andreas Barg, Eugene S Polzik, and Albert Schliesser. Ultracoherent nanomechanical resonators via soft clamping and dissipation dilution. Nature Nanotechnology, 12(8):776–783, 2017.

[47] Luis Guillermo Villanueva and Silvan Schmid. Evidence of surface loss as ubiquitous limiting damping mechanism in sin micro-and nanomechanical resonators. Physical Review Letters, 113(22):227201, 2014.

[48] Andreas Wallucks, Igor Marinković, Bas Hensen, Robert Stockill, and Simon Gröblacher. A quantum memory at telecom wavelengths. Nature Physics, 16(7):772–777, 2020.

[49] Matthew J Weaver, Brian Pepper, Fernando Luna, Frank M Buters, Hedwig J Eerkens, Gesa Welker, Blaise Perock, Kier Heeck, Sven de Man, and Dirk Bouwmeester. Nested trampoline resonators for optomechanics. Applied Physics Letters, 108(3):033501, 2016.

[50] Dalziel Joseph Wilson. Cavity optomechanics with high-stress silicon nitride films. PhD Thesis, 2012.

[51] Ya-Tang Yang, Carlo Callegari, XL Feng, Kamil L Ekinci, and Michael L Roukes. Zeptogram-scale nanomechanical mass sensing. Nano Letters, 6(4):583–586, 2006.

[52] P-L Yu, K Cicak, NS Kampel, Y Tsaturyan, TP Purdy, RW Simmonds, and CA Regal. A phononic bandgap shield for high-q membrane microresonators. Applied Physics Letters, 104(2):023510, 2014.

[53] P-L Yu, TP Purdy, and CA Regal. Control of material damping in high-q membrane microresonators. Physical Review Letters, 108(8):083603, 2012.

[54] Mingyun Yuan, Martijn A Cohen, and Gary A Steele. Silicon nitride membrane resonators at millikelvin temperatures with quality factors exceeding 108. Applied Physics Letters, 107(26):263501, 2015.

[55] F Zhou, Y Bao, DA Long, R Madugani, JJ Gorman, and TW LeBrun. Testing of an optomechanical accelerometer with a high-finesse on-chip microcavity. In CLEO: QELS_Fundamental Science, pages JW2A–4. Optical Society of America, 2019.

[56] Feng Zhou, Yiliang Bao, Ramgopal Madugani, David A Long, Jason J Gorman, and Thomas W LeBrun. Broadband thermomechanically limited sensing with an optomechanical accelerometer. Optica, 8(3):350–356, 2021.

[57] BM Zwickl, WE Shanks, AM Jayich, C Yang, AC Bleszynski Jayich, JD Thompson, and JGE Harris. High quality mechanical and optical properties of commercial silicon nitride membranes. Applied Physics Letters, 92(10):103125, 2008.